Monte Carlo Simulations of Chemical Vapour Deposition Diamond Detectors

Florentina Baluti

A thesis submitted in partial fulfilment
of the requirements for the degree of
Master of Science
in
Medical Physics
at the
University of Canterbury
Christchurch, New Zealand
2009

Abstract

Chemical Vapour Deposition (CVD) diamond detectors were modelled for dosimetry of radiotherapy beams. This was achieved by employing the *EGSnrc* Monte Carlo (MC) method to investigate certain properties of the detector, such as size, shape and electrode materials. Simulations were carried out for a broad 6 MV photon beam, and water phantoms with both uniform and non-uniform voxel dimensions. A number of critical MC parameters were investigated for the development of a model that can simulate very small voxels. For a given number of histories (100 million), combinations of the following parameters were analyzed: *cross section* data, *boundary crossing algorithm* and the *HOWFARLESS* option, with the rest of the transport parameters being kept at default values. The MC model obtained with the optimized parameters was successfully validated against published data for a 1.25 MeV photon beam and CVD diamond detector with silver/carbon/silver structure with thicknesses of 0.07/0.2/0.07 cm for the electrode/detector/electrode, respectively.

The interface phenomena were investigated for a 6 MV beam by simulating different electrode materials: aluminium, silver, copper and gold for perpendicular and parallel detector orientation with regards to the beam. The smallest interface phenomena were observed for parallel detector orientation with electrodes made of the lowest atomic number material, which was aluminium. The simulated percentage depth dose and beam profiles were compared with experimental data. The best agreement between simulation and measurement was achieved for the detector in parallel orientation and aluminium electrodes, with differences of approximately 1%.

In summary, investigations related to the CVD diamond detector modelling revealed that the *EGSnrc* MC code is suitable for simulation of small size detectors. The simulation results are in good agreement with experimental data and the model can now be used to assist with the design and construction of prototype diamond detectors for clinical dosimetry. Future work will include investigating the detector

response for different energies, small field sizes, different orientations other than perpendicular and parallel to the beam, and the influence of each electrode on the absorbed dose.

Acknowledgements

This thesis was completed with the support of people involved either directly or indirectly. They are those to whom I dedicate this work.

My thanks and gratitude to my thesis advisor Dr. Juergen Meyer who helped me with the scientific work. He was always available to resolve issues related to my research. My regards to my clinical supervisor Dr. Hossain Deloar. Without his help and knowledge this thesis would not be finalized. I would also like to acknowledge Dr. Jenny Lydon for her support and supervision at the beginning of the project. My thanks to my previous clinical director Dr. Richard Tremewan who inspired me with the subject of the thesis. A special thanks to Dr. Mark Bird for his support, his helpful comments on physics, and encouragement during the work. I would also like to thank Dr. Stuart Lansley and Greg Betzel for their comments on my work, as well as my colleagues for their patience and understanding.

I would like to thank my mother for her full and unconditioned support, my husband Silviu and my children, as they spent an impressive amount of time without me around. To my friends Gwenda, Virginia, Rose and Mele. Thank you for your support. I hope I will be able to return at least part of it.

Contents

Glossary of terms and abbreviations

521icru.pegs4	*ICRU cross section* data file for low energy photon beam
700icru.pegs4	*ICRU cross section* data file for high energy photon beam
ASCII	American Standard Code for Information Interchange
AVM	Arteriovenous malformation
BEAMnrc	Monte Carlo simulation system for modelling radiotherapy sources
BCA	Monte Carlo *boundary crossing algorithm*
CDF	Cumulative distribution function
CT	Computerized Tomography
CVD	Chemical Vapour Deposition
Debian	Computer operating system composed of free and open source software
DOSXYZnrc	*EGSnrc* user interface for 3D absorbed dose calculations
DOSXYZ_SHOW	Monte Carlo user interface for the display of isodose distributions
ECUT	Electron cutoff energy
EGS	Electron Gamma Shower
EGSnrc	Monte Carlo code used to simulate charged particle and photon transport
EXACT	Non-default option of the *EGSnrc* user code *boundary crossing algorithm*
FWHM	Full width at half maximum
GEANT	GEometry ANd Tracking
HPHT	High Pressure High Temperature
HOWFARLESS	Monte Carlo parameter used for simulating charged particle and photon transport inside homogenous phantoms

ICRU	International Commission for Radiation Units
IMRT	Intensity modulated radiation therapy
LET	Linear energy transfer
MC	Monte Carlo
MCNPX	Monte Carlo *N-Particle eXtended*
MLC	Multileaf collimator
MOSFET	Metal-oxide semiconductor field effect transistor
MU	Monitor unit
PCUT	Photon cutoff energy
PDD	Percentage depth dose
PDF	Probability density function
PEGS4	Monte Carlo *cross sectional* data file used for material simulation
PRESTA-I	Default option of the *EGSnrc* user code *boundary crossing algorithm*
SRS	Stereotactic radiation surgery
SRT	Stereotactic radiation therapy
SSD	Source to surface distance
STATDOSE	Monte Carlo user interface for 3D dose evaluation in beam profiles
TLD	Thermoluminescence dosimeter
Ubuntu	Debian-derived computer operating system based on GNU/Linux
XVMC	*XrayVoxel* Monte Carlo

Chapter I

Introduction

Cancer is a major cause of mortality in developed countries. "Cancer is New Zealand's leading cause of death, according to the latest New Zealand Health Information Service (NZHIS) official figures" [1]. There are three different modalities of cancer treatment. One is radiotherapy, with the other two being surgery and chemotherapy.

1.1 Radiotherapy

Radiation therapy has been used as a cancer treatment for over 100 years. Radiation therapy is referred to as radiotherapy, radiation oncology or therapeutic radiology. It is a proven method for controlling malignancies and for prolonging the

life of individuals who would otherwise die from their cancer. Radiation therapy is used in more than half of all cancer treatments, and in some cases it is the preferred and most effective treatment of all. In other cases, it is used in combination with chemotherapy or surgery. Radiotherapy treatment can cure some cancers and can also reduce the chance of a cancer returning after surgery. It also can be used as a palliative to reduce cancer symptoms. Radiotherapy works by destroying the cancer cells in the treated area with high energy x-rays or high energy electrons [2]. The ionizing radiation damages the cells' DNA, blocking their ability to divide and proliferate. All the cells suffer from radiation, but healthy cells can adapt over successive regenerative cycles. Malignant cells do not possess this adaptation mechanism and thus do not survive.

Radiation treatment involves four basic steps: initial consultation and diagnosis; simulation for tumour and critical structure localization; treatment planning, and treatment delivery. Radiation therapy can be delivered externally from a high energy machine and/or internally using brachytherapy, by implanting radioactive sources in or near the cancerous tissue.

1.1.1 Importance of accurate dose calculation

The ideal radiotherapy treatment delivers a high dose of radiation to the tumour and a minimal dose to the surrounding normal tissue. To obtain full advantage of the radiation therapy treatment, it is essential that the absorbed dose delivered to all the irradiated tissues is predicted accurately. This can be achieved with exact radiation dosimetry. Radiation dosimetry represents an important aspect of cancer treatment as the human body consists of different tissue densities, cavities and in some cases foreign materials such as metallic prostheses [3].

Optimal therapeutic benefits can be reached by increasing the dose to the target volume and minimizing the dose to the normal tissues. Some high dose treatments are limited by the radiation toxicity capacity of healthy tissues which lie close to the target tumour volume. In this case it is difficult to increase the prescribed dose to

improve tumour control without increasing adjacent tissue complications. This is illustrated in Figure 1.1.

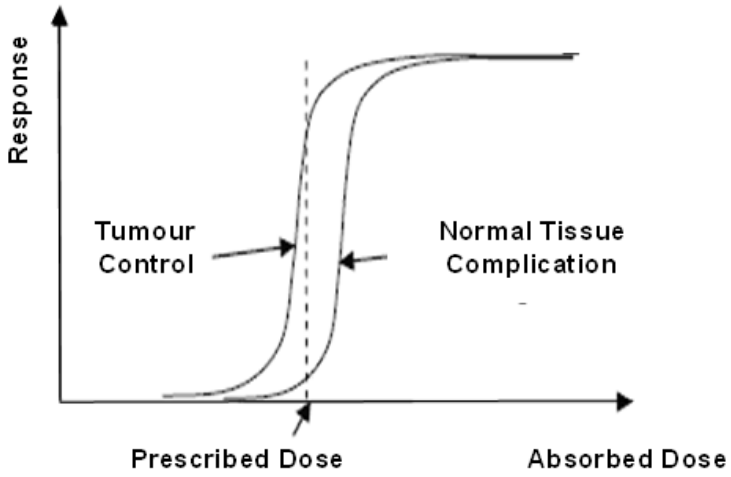

Figure 1.1 Dose response curves for tumour and normal tissue

Optimization of the dose response requires correct localization of the cancerous tissues and of the sensitive normal tissues, as a small change in dose can have a large negative impact on the normal tissue and on tumour control.

Significant progress in imaging technology in the last two decades has influenced the ability to recognize and localize the critical volumes and determine their densities. Moreover, radiation therapy treatment delivery systems have advanced, and target volumes can be irradiated with very high accuracy. The combination of superior imaging procedures and beam modulation (aperture and intensity) techniques allows the radiation dose to be precisely conformed around the targeted tissue [4].

1.2 Dosimetry for modern radiotherapy

High precision radiotherapy techniques, such as intensity modulated radiotherapy (IMRT), stereotactic radiotherapy (SRT), stereotactic radiosurgery (SRS) and

tomotherapy involve the superposition of several uniform but narrow beams. These techniques require very firm immobilisation of the patient and incorporation of radiological examination in the treatment planning for precise definition of the target. Modern radiotherapy techniques use modulated beams in terms of dimensions, intensity and/or energy [4].

The IMRT concept is to produce a dose distribution that matches closely to the planned target volume and limits damage to normal tissue, reducing toxicity and increasing the dose delivered, which improves tumour control and survival. Comparative planning investigations demonstrate that superior dose distribution can be achieved using IMRT for various tumour sites, such as the prostate, the breast, the reproductive system, the head and the neck [5].

In IMRT, the dose intensity varies within each of the many conformal fields, allowing highly individualised dose gradients throughout the treated volume. To deliver the planned dose distributions, intensity profiles are commonly translated into various multileaf collimated segments using multileaf collimators (MLC). Delivery of small segments with at least one dimension smaller than 2 cm is regularly required in the IMRT technique. To be able to calculate dose distribution and monitor units (MUs) for such small segments accurately, high-resolution absolute and relative dosimetry is important [2].

In the “step and shoot” IMRT technique, the exact position of the MLCs depends on the penumbra calculated by the IMRT planning engine for segments. An inaccurate calculation of the penumbra can result in cold and hot spots between two adjacent segments. Thus, it is important to provide an IMRT planning engine with accurate dosimetric data [6].

The aim of stereotactic radiotherapy (SRT) and stereotactic radiosurgery (SRS) techniques is to deliver a reasonably large radiation dose to an intracranial volume, in precisely the right place. SRT and SRS are important clinical tools for the

treatment of small lesions in the brain, including arteriovenous malformations (AVMs) and pituitary adenomas.

Radiation beams with a diameter of 4 cm or less are normally used in SRT/SRS to deliver a single large dose fraction to a small target volume with steep dose gradients around the target periphery. Correct determination of the penumbra of radiosurgery profiles is critical to avoid complications in organs at risk adjacent to the tumour. For SRT/SRS beams, lateral electronic equilibrium does not exist in a large proportion of the beam; hence, accurate dosimetry plays an important role in reaching modern radiotherapy's aim of delivering a high dose to the target volume by limiting damage to the normal tissue [6].

Dose measurement of small beams is more difficult and complicated than that for conventional beams because of two factors: the lack of equilibrium in lateral charged particles which leads to steep dose gradients in the penumbra region, and the relationship between detector size and field dimension [7].

Adequate dosimetry gives the assurance that the planned dose is the same as the delivered dose to the patient. For example, the consequences of inaccurate measurements of the penumbra can result in errors of determining the field edge of the treatment and delivered dose [8]. Consequently the most problematic issues encountered are related to the inaccuracy of the penumbra measurements which can result in errors when shaping the treatment field edge and delivered dose.

One of the most important criteria in the choice of detector in narrow field dosimetry is the detector's size [9]. It must be small enough to minimize perturbations of the particle fluence, but large enough to be subjected to a large number of interactions so that it will yield a signal with a high signal-to-noise ratio. In the case of an inappropriate detector or experimental geometry, there might be a significant dose fall off within the sensitive volume from the centre to the periphery of the detector. This complicates the interpretation of central axis measured dose values [7].

Additionally, when making measurements away from the central beam axis, the detector might not be able to resolve correctly the existing steep dose gradient because of lateral electronic disequilibrium [9]. The choice of the detectors depends on the quantity that needs to be measured, and that quantity can be either central axis dose measurements or beam profiles dose distributions [10].

Beam profiles and central axis dose measurements are required as input data for the treatment planning computer. Accurate determination of these parameters leads to accurate determination of the three dimensional dose distribution produced by the treatment planning system. As mentioned above, lateral electronic disequilibrium and steep dose gradients are characteristics of small SRT beams.

The existence of the lateral electron disequilibrium has consequences. One is that, as the field size is reduced, the output drops dramatically, and the cross beam profile may be flat only over a small fraction of the full width at half maximum (FWHM). Another consequence is that the dependence of the output, or dose rate at a point on the central axis, on the source to point distance (SPD) may not follow the inverse square law for large values of SPD. Thus, the dose rate on the central axis decreases more rapidly with SPD than the inverse square law would predict.

In the published literature, most data acquisition for a small field size is based on diodes, photographic and photochromic films, and partially on thermoluminescence dosimetry (TLDs) [11].

Typical radiation detectors, such as the 0.6 cm^3 Farmer type ion chambers, are inappropriate for performing dosimetry for small radiation fields because of their relatively large sensitive volumes, particularly when electronic disequilibrium exists across the whole field [12]. Therefore, small chambers with sensitive volumes smaller than 0.1 cm^3 are generally used for absolute dose verification. Film dosimetry could be a preferred technique in the dosimetry of these very small fields, but film is energy dependent and also suffers from variations in the film coating and processing conditions which make it unreliable. The use of radiochromic films may

overcome some of the problems associated with conventional radiographic films. Better tissue equivalence, higher spatial resolution, and room light handling are the main advantages of radiochromic films. The disadvantage of these films is nonlinearity of the response for doses in the clinical range. To achieve acceptable precision (+/- 2%), much higher doses are necessary (around 100 Gy). Silicon diodes, because of the very small size of the sensitive volume (60 μm thickness and 2.5 mm width), are the common choice in dosimetry of SRT beams [12, 13]. However, energy, dose rate, and directional dependence of response are negative factors in this application.

Diamond detectors, because of the near tissue equivalence of carbon, should act as suitable detectors, although their dose rate dependence could affect the result. If corrected, they produce better results than the more commonly used diode and film dosimetry techniques [14]. The diamond detector is considered to be an improved alternative to the above detectors used for small field dosimetry [15].

The measurement of the dosimetric characteristics of small diameter radiation beams requires the use of a small volume detector but there is no general agreement on which detector should be used [16]. A recent comparative dosimetry study of small photon beams has been completed for PinPoint ionization chambers, solid state detectors such as Si-diode, MOSFET, and diamond. It was reported that, by applying a linear sensitivity correction, all the above detectors offer the same signal for a field size equal to or larger than 8 mm [16].

Dose measurement of small beams is more difficult and complicated than for conventional beams [17]. To obtain an accurate dose delivery, the dose at any point inside the patient needs to be calculated and related to the calibration dose. Therefore, the dose at specific locations in the radiation field has to be measured in a phantom prior to treatment for verification of the treatment plan and quality assurance.

1.2.1 Diamond detector

Diamond detectors are used in small field dosimetry as reported in different studies, and they are considered to provide reliable data [8, 18, 19]. However, natural diamonds with good, reproducible electrical properties are difficult to find and this makes them very expensive. The alternative is the synthetic diamond produced by means of Chemical Vapour Deposition (CVD) [20, 21].

The main characteristics of the natural diamond are [22]:

- large band gap which ensures low dark currents and low noise;
- high carrier mobility which permits a fast dynamic response;
- high sensitivity that gives small dimensions and high resolution;
- strong atomic bonding which indicates radiation hardness;
- it is chemically inert, non-toxic, and has a low atomic number;
- tissue equivalence which implies no need of correction for dose determination;
- the ability to detect all types of radiation.

The main drawbacks of the natural diamond detector are the time consumed in the selection of the right diamond stone, cost, as well as the poor intersample reproducibility [20].

The influence of the impurities naturally implanted in the sensitive volume is clear. Some impurities are necessary in order to increase the signal linearity with the dose rate of the detector [20]. However, an excess of impurities can decrease detector sensitivity, and increase the polarization effect. The polarization effect is caused by impurities which act as traps and create an electric field that is opposite to the applied bias voltage [23]. This is the main cause of the natural diamond detector's nonlinear dose rate dependence.

Consequently only natural diamonds with low concentration of nitrogen can be used for dosimetry. This adds to the lack of immediate availability, and cost increase [21].

1.2.2 Chemical Vapour Deposition (CVD) diamond

Synthetic diamonds can be produced by two methods: High Pressure High Temperature (HPHT), and Chemical Vapour Deposition (CVD). HPHT is more widely used because of its low cost compared with the CVD method. The CVD process creates plasma on the top of a silicon substrate. Carbon atoms are deposited on the substrate to form a diamond structure. CVD diamonds can be grown with different thicknesses and dimensions by changing the growth parameters. CVD diamond films are produced with similar electrical and thermal properties as the natural diamonds.

It has been demonstrated that the CVD diamond has sufficient sensitivity to be used as a dosimeter, when compared with other commercially available devices [13]. In the CVD method, the grain size, layer thickness and level of impurities can be controlled. A well controlled growth of a CVD diamond with desired properties can be achieved at low cost.

The main advantage of the CVD diamond films over the current and commercial dosimeter materials is the biological compatibility with human tissue (Z_{eff} = 6.0, close to Z_{eff} = 7.5 of human tissue) [24]. At the same time, the CVD diamond is non toxic, and can be grown at low cost and with features suitable for dosimetric use. CVD films have shown promising dosimetric properties and the possibility of their clinical use is growing [25].

Other advantages of the CVD diamond are: high resistance to radiation damage, high sensitivity and stability, good time resolution and low leakage current, electrical insulation properties, stability and robustness and the fact that they can be produced in a small size [24].

These characteristics illustrate very good reasons for synthetic diamonds to be used as dosimeters. However, the synthetic films also have some drawbacks. These are [24]:

- dynamic response (pumping effects, slow rise and decay times);
- linear energy transfer (LET);
- dose rate dependence.

During the investigation of CVD diamonds, it was found that they have a slow dynamic response, of around few seconds. The speed of the dynamic response can be increased by controlling the impurities in the growth phase, optimising the electrode contact's material and thickness, as well as improving the process of deposition by filling superficial traps by preirradiation [20, 26].

The CVD diamond detector, like the natural diamond, is not very easy to use. It requires preirradiation [24], it can lose the equilibrium condition if it is not used for a long time, and has a dose rate dependence that needs to be accounted for [26]. Futher analysis of the CVD diamond detector is needed. Cirrone et al. [24] concluded that the following should be investigated: current-voltage characteristics, preirradiation effects, stability, dose dependence, dose-rate dependence, and energy dependence.

Due to its small size, the CVD diamond detector can be designed to introduce negligible perturbations to the radiation field and the dose distribution in the phantom, but detector construction materials need to be carefully selected as they may bring in severe fluence perturbation and angular dependence, resulting in erroneous dose readings.

In a significant piece of research, Gorka et al. investigated interface phenomena between high and low atomic number materials using MC code *PENELOPE* [27].

The aim of this work was to use MC methods to develop a model to further investigate the properties of the CVD diamond detector.

1.3 Research motivation

Research has revealed the necessity of a detector with small dimensions, tissue equivalence, high sensitivity, and good spatial resolution for regions of large dose gradients.

A team of scientists and students from the University of Canterbury has developed a synthetic diamond detector for clinical use [28, 29]. The first prototypes developed are in a sandwich-like structure (metal, diamond, metal). The electrode material was deposited on the diamond film using thermal evaporation. Investigations of the electric and dosimetric characteristics of these devices are in progress. The aim was to design a detector with the above characteristics, which also provides a linear response to an absorbed dose and has no, or minimal, dependency on dose rate, energy and orientation.

A fundamental aspect of the diamond detector design is the selection of optimal structural materials (electrodes, wires, contacting glue and encapsulation) [27]. These structures can introduce significant fluence perturbations and angular dependence that can result in inaccurate dose readings. Interface phenomena between high and low atomic number materials are produced between metallic electrodes and diamond films. The direction of the radiation field can influence the detector signal.

Knowledge of fluence perturbation and its influence on the signal of the detector are relevant to the construction of an energy independent, tissue equivalent CVD diamond detector and quantification of the fluence perturbation correction. Good knowledge will give an accurate theoretical representation of the dose distribution for the purpose of validating the performance of the detector.

Advances of computer technology in recent years have provided very fast computers at low cost [9]. This makes the use of the MC method widely available for investigations.

The aim of the work presented in this thesis was to investigate the CVD diamond detector's physical and dosimetric characteristics using the MC technique. The *EGSnrc/BEAMnrc* code was chosen to investigate the following characteristics:

- dimensions of the detector and electrodes,
- electrode materials,
- orientation of the detector in the photon radiation beam,
- depth dose and profiles,

for a better understanding of CVD diamond detector design and behaviour.

The MC method is widely accepted as more accurate in comparison with deterministic or analytical calculations. It provides information which is not extractable from physical measurements and offers a "virtual" experimental platform.

1.4 Outline of approach

The next chapter includes a brief history and description of the MC method, its use in radiation therapy, the basics of the method considered in this project, as well as a short description of the dose calculation code and other user codes used in this work.

The steps involved in the development of a Monte Carlo model for the simulation of a small size CVD diamond detector with thin electrodes are presented in Chapter III.

Validation of the CVD diamond detector simulations is done in Chapter IV by comparison with experimental data for absorbed dose at different depths inside a water phantom, and by lateral beam profile evaluation.

The conclusions to this work are presented in Chapter V, together with sugestions for future work.

Chapter II

Monte Carlo

2.1 Brief history

Monte Carlo methods have been used since the second half of the nineteenth century, but only in the past few decades has the technique gained the status of a numerical method capable of addressing the most complex applications [30].

The Monte Carlo method is designed to solve problems consisting of many independent smaller ones (like the spin of a roulette wheel, or toss of dice at a casino), using a random number generator. Its core idea is to use random samples of parameters or inputs to explore the behaviour of a complex system or process.

The method's name was adopted from the Monte Carlo casino which was one of the best known venues for roulette and games of chance in Monaco. The fair roulette wheel is one of the earliest random number generators. The use of randomness and the repetitive nature of the Monte Carlo process are analogous to the activities conducted at a casino.

In the early part of the twentieth century the method was used for teaching and confirming verification (the technique was employed to test previously understood deterministic problems) and very rarely in research of original discoveries [31].

In the 1930s Enrico Fermi used a random method to calculate the properties of the newly-discovered neutron, and later designed the FERMIAC, an inspired analogue device to implement studies in neutron transport [32].

In the 1940s a formal foundation for the Monte Carlo method was developed by John von Neumann, who established the mathematical basis for probability density functions (PDFs), inverse cumulative distribution functions (CDFs), and pseudorandom number generators. The work was done in collaboration with the mathematician Stanislaw Ulam. In 1947 von Newmann outlined the possible statistical approach to solving the problem of neutron diffusion in fissionable material based on Ulam's concept of "lucky numbers".

Monte Carlo methods formed the core of the simulations required for the Manhattan Project. Applications resulting from this project included the design of shielding for reactors [30].

In the 1950s Monte Carlo was used in the early work at Los Alamos as a research tool in the development of the hydrogen bomb, the work involving direct simulations of the probabilistic problems concerned with random neutron diffusion in fissile material [32].

The scientists faced physics problems, such as models of neutron diffusion that were too complex for an analytical solution, so they had to be evaluated numerically. However, their models involved so many dimensions that exhaustive numerical evaluation was extremely slow. Monte Carlo simulation proved to be effective at finding solutions to these problems [32].

Around 1970, the newly developing theory of computational complexity started to provide a precise and convincing basis for the use of the Monte Carlo method [33]. Simulation time has been shortened, the charged particle transport simulation using the Monte Carlo method being possible to be accomplished within reasonable time frames [32].

Since that time, Monte Carlo methods have been applied to an exceedingly diverse range of problems in science, engineering, finance and business applications, in almost every industry [34].

2.2 The Monte Carlo method

The Monte Carlo method provides solutions to mathematical problems by performing statistical sampling experiments on a computer.

The main components of the Monte Carlo method are [33]:

- the probability distribution functions describing the physical system;
- the random number generator which is a source of uniformly distributed random numbers;
- the sampling rule which is a recommendation for sampling the probability distribution function;
- the variance reduction techniques, which are methods for reduction of the computational time for Monte Carlo simulation;

- the scoring (or tallying), which represents the outcomes of the interest quantities.

Monte Carlo has the ability to simulate the tracks of individual particles for radiation transport problems. This is done by sampling appropriate quantities from the main probability distributions of the individual physical processes. Quantities such as particle fluence, energy spectrum and absorbed dose distribution can be calculated by simulating a large number of particle histories [33].

A number of publications, i.e. [35-37], have shown that the Monte Carlo method has many applications in medical radiation physics, especially in radiation therapy physics. The Monte Carlo techniques have accurately accounted for the density and atomic number variations within the medium, back scatter or scatter perturbations. Monte Carlo simulation of radiation transport is more accurate than deterministic or analytical calculations particularly under conditions of electronic disequilibrium, mainly due to the complexity of electron transport.

In radiotherapy Monte Carlo provides a virtual experimental platform of various beam configurations on a virtual phantom or patient, and facilitates detailed understanding of radiation physics, for example stages of radiation detection in a detector [38]. The major drawbacks of the Monte Carlo for radiation transport modeling technique are the computing time and the need for a detailed knowledge of the incident radiation beam [34].

2.3 Physics theory of Monte Carlo technique

The physics of photon and electron interactions in matter are known, but there is no logical expression to describe particle transport within a medium. Electrons can create both photons (for example Bremsstrahlung) and secondary electrons. Photons can produce both electrons and positrons through Compton scattering and pair production. Any given particle moving through a material has a probability of undergoing each of the interactions, with a range of possible outcomes. Particles

produced by one interaction undergo subsequent changes, until all the energy of the incident radiation is absorbed by the target material. Monte Carlo models the particles and their subsequent changes by sampling every undertaken event, and discarding the particles either with energies below the cutoff level or which are outside the simulation, as shown in Figure 2.1.

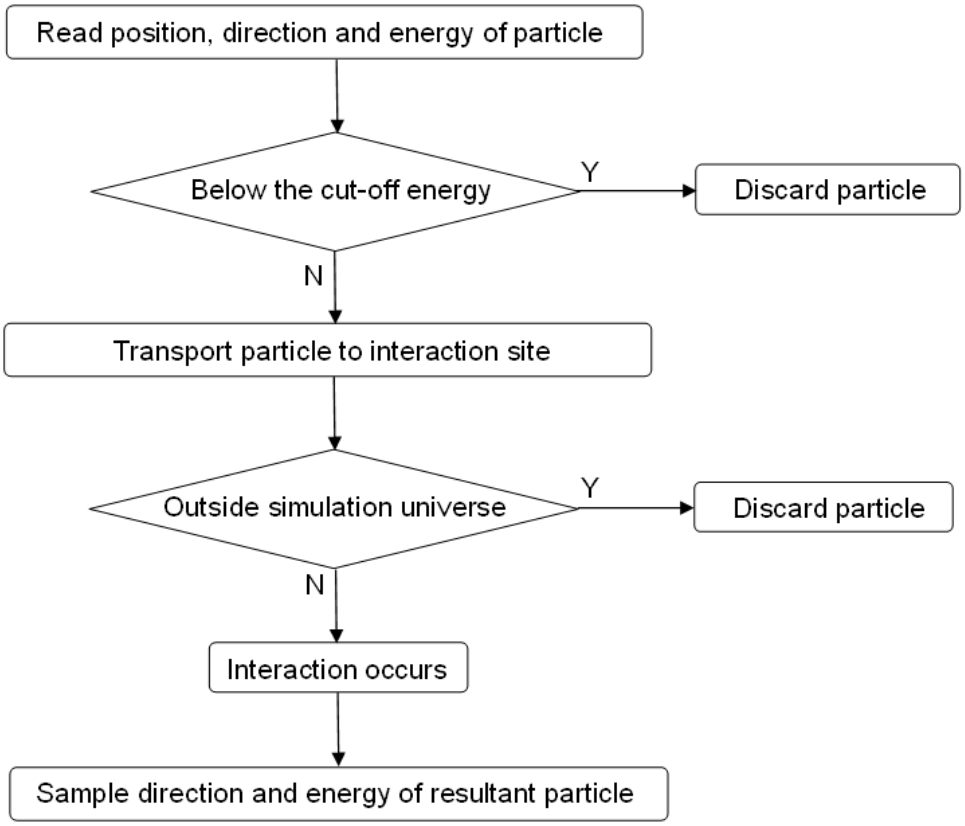

Figure 2.1 Steps of a typical analogue transport process of primary and secondary particles for regular geometry. The analogue transport samples every single event explicitly. Simulation of the photons is usually done in this way [39].

Monte Carlo techniques are extensively used in radiation therapy applications because they can precisely simulate the transport of photons and electrons in matter, and they use scattering models for different interaction processes and for a large range of energies. Numerical tabulated values and calculated cross sectional data are combined in the scattering models [40].

Photons undergo a limited number of interactions before they are absorbed and the interaction processes are properly described, which makes it easy to simulate all interactions directly [38].

On the other hand, high energy electrons lose a very small part of their energy in each interaction, and as a consequence electrons can undergo a very large number of interactions before being totally absorbed. Therefore, given that the number of Coulomb interactions with atomic nuclei is so large, direct Monte Carlo simulation for electron beams is less practical than the simulation of photon beams [40].

2.4 Monte Carlo modelling in radiotherapy

The Monte Carlo method is widely accepted as the most accurate method for modelling radiotherapy treatments [40-42] and has started to become more accesible since technological advances have made very fast computers available at low cost. Parallel processing can increase the CPU power and shorten simulation times.

Several Monte Carlo programs have been used for radiation therapy simulations, including Monte Carlo *N-Particle eXtended (MCNPX)* [43], *XrayVoxel* Monte Carlo *(XVMC)* [44], *GEometry ANd Tracking (GEANT)* [45] and *Electron Gamma Shower (EGS)* [38].

2.4.1 EGSnrc code

The first version of the *EGS* Monte Carlo code was written in the early 1960s, and later on developed into *EGS4* which further developed into *EGSnrc* for the Linux operation system platform and then *EGSnrcMP* by the group of National Research Council (NRC) Canada, where MP stands for multi-platform [38].

The *EGSnrc* code uses similar sets of subroutines as *EGS4*. It has been designed to simulate the particles' (electron/photon) various interactions through the matter for the electron energy range of 10 eV to 100 GeV and for photon energies of 1 eV to 100 GeV [38]. *EGSnrc V4* has the power to calculate exactly what the user needs by applying variance reduction techniques that considerably speed up the simulation [46], and was used throughout all the simulations in this project.

2.4.2 BEAM user code

Monte Carlo modelling of radiotherapy systems involves two phases: simulation of the linear accelerator head using *BEAM* code, and simulation of the patient/phantom using *DOSXYZ* code. *BEAM* was designed to model all types of radiotherapy accelerators, as well as Co60 units and X-ray units. The code is written in MORTRAN3, a Fortran 77 pre-processor which is used for the *EGS4* system [38]. A complete *EGS/BEAM* run includes the linac head simulation, dose delivered to the patient/phantom simulation, and the analysis of the dose distribution.

The *BEAMnrc* code can be used to simulate the linear accelerator models for various vendors and allows the simulated information of the particles from the linear accelerator to calculate doses in voxel based water or CT phantom.

Given that the accelerator head includes several different components: the target, the flattening filter, the ion chamber, the mirror, the field definition system and the crosshair, as shown in Figure 2.2, the *BEAM* user code has to provide a variety of component modules (CMs) for the simulation of the linac's head. Some of the CMs generally employed are: *SLABS, FLATFILT, CHAMBER, JAWS, CONS3R, MIRROR,* which allow the reproduction of complicated head geometries. These modules are predefined for linear accelerator components but they are customizable and can also be used for other purposes.

The *BEAM* code models the therapy source with the Z axis taken as the beam axis and usually the origin is defined as the centre of the beam as it exits from the

accelerator. Each component module is contained between two planes which are perpendicular to the Z axis, and which cannot overlap.

The simulation of the linear accelerator model is vendor specific. In the modelling process the information of the linear accelerator components which includes materials, positions, shape and dimensions is required from the manufacturer [9].

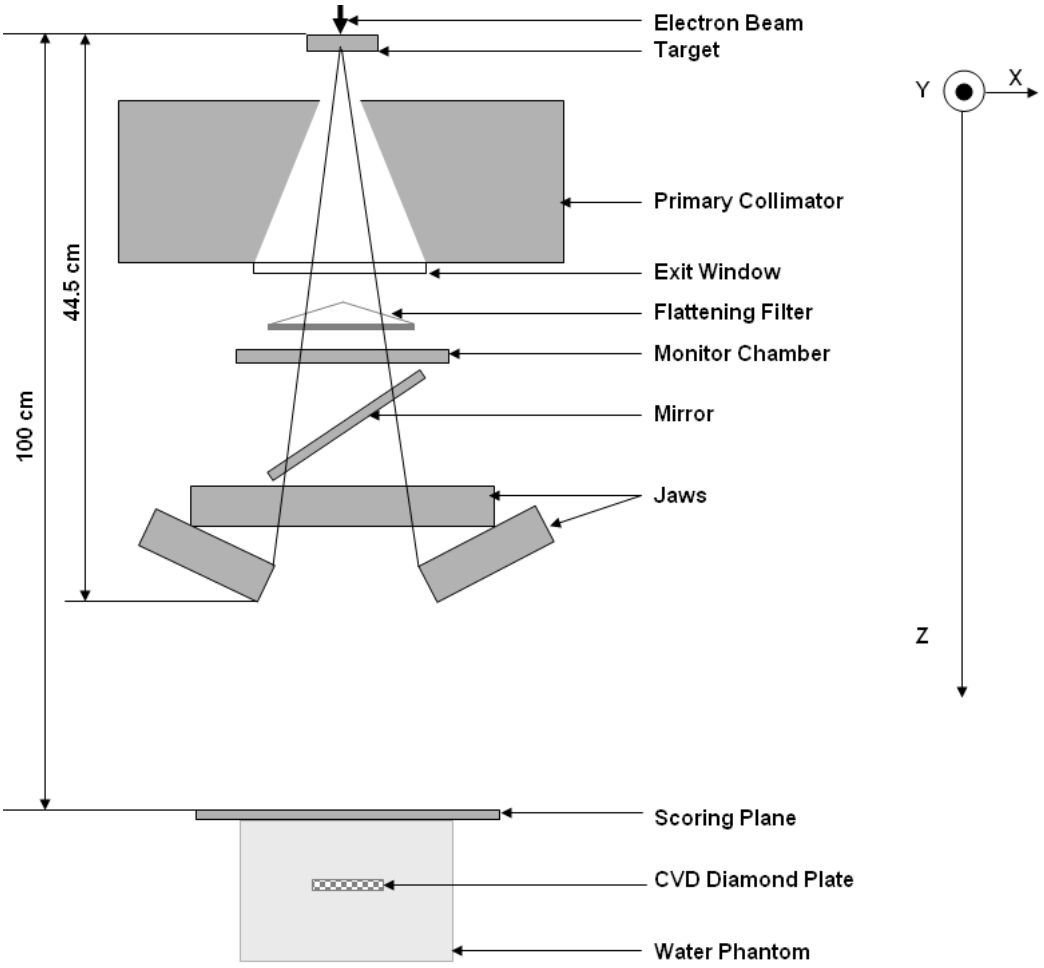

Figure 2.2 Schematic diagram of the linear accelerator in Monte Carlo modelling with the CVD diamond detector at an arbitrary position in a water phantom

The input file contains the details about the accelerator, for example: the number of scattering foils, their location (specifying the relative distances), and the thicknesses and materials from which they are made. Moreover, it contains all the parameters

that control the radiation transport modelling, and also selects and controls the various variance reduction techniques to be used [41].

The steps used in linear accelerator simulations by using *BEAMnrc* are shown in Figure 2.3.

BEAM has three major forms of output: the *listing file*, the *phase space data* file, and the *graphics output* file. The final step of the linac simulation is the output analysis, especially of the *raw phase space* file.

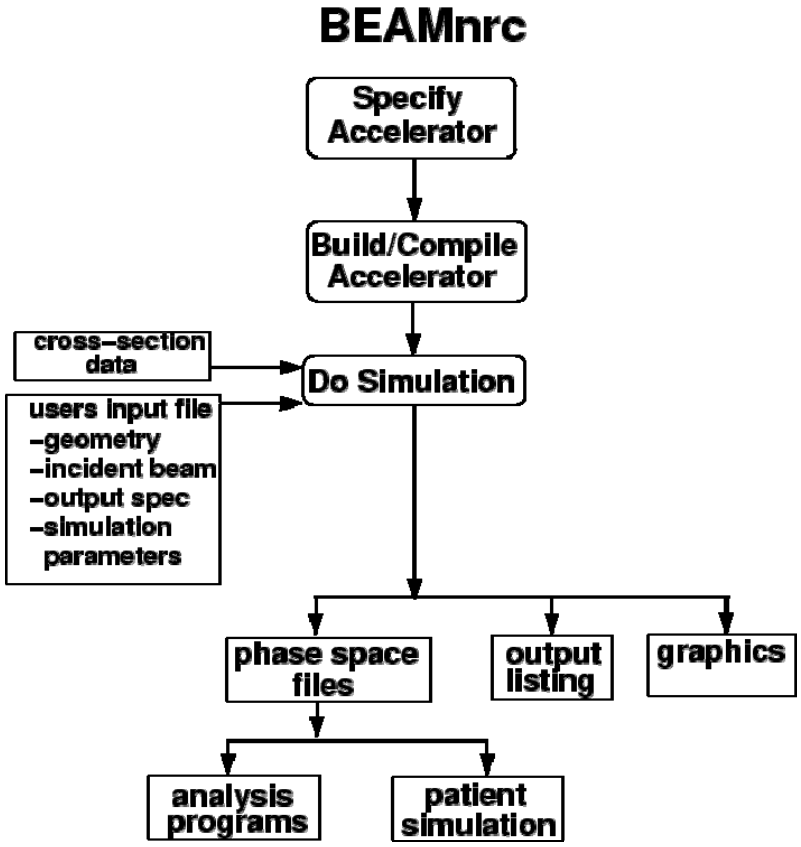

Figure 2.3 The steps involved in using *BEAMnrc* system, from reference [42]. To specify an accelerator means to define an ordered set of component modules (CMs) to be used in the simulation.

The *phase space data* file contains information about each individual particle crossing the scoring planes, such as position, direction of motion, energy or momentum, charge, and history tag. It can be produced at any specified plane in the model. This file is usually the most important output. Scoring planes are at the back plane of a CM perpendicular to the Z axis and they contain scored particle fluences, average energies and average angles, as well as the dose. The information from the *phase space* file can be re-used by the *BEAM* code itself in further calculations. It also can be used as an input file to determine the dose distribution in a model built from the CT scan of the patient, or used to characterize the beam in a more compact way.

The *BEAM* code used for the simulation of the accelerator whose *phase space* file output was employed in this research was developed as an *EGS4* user code that is capable of complex linac geometric coding [42] by the National Research Council of Canada (NRCC), originally part of the OMEGA (Ottawa Madison Electron Gamma Algorithm) project. The phantom was simulated with the *DOSXYZ* code, part of the same *EGS4* OMEGA project.

The actual accelerating waveguide and associated beam line components are not usually modelled. Electron beam characteristics may fluctuate, and this can influence the physical characteristics of the final photon or electron beams used in treatment, consequently controlling the dose distribution in the patient.

Christchurch Hospital Monte Carlo group members have previously modelled their linear accelerators for different energies. The particle transport through the accelerator components have been stored in *phase space* files set at Z = 100 cm from the linac head [37] (Figure 2.2). The *phase space* file contains information concerning particles including position (x, y, z), direction (X, Y, Z), energy, charge, weighting, and origin, and serves as the source for the water phantom simulations using *DOSXYZ*.

2.4.3 DOSXYZnrc user code

DOSXYZ is a general purpose Monte Carlo *EGS* user code for 3D absorbed dose calculations. During this work, the 6.6 version of *DOSXYZ* was used. This is the *DOSXYZnrc* version, part of the *EGS4* OMEGA project previously mentioned.

DOSXYZnrc simulates the transport of photons and electrons in a cartesian volume and scores the energy deposition in the designed volume element (voxel). *DOSXYZnrc* was employed to calculate the dose distribution in a water phantom made of customizable voxles based on 3D cartesian coordinates, and to simulate dose delivered to the CVD diamond detector.

To obtain the absorbed dose in *DOSXYZnrc*, the modelling requires a 3D phantom and a radiation source. Extension of the 3D phantom file name is *.egsphant*. The geometry of the phantom is composed of a linear volume with the (XZ) plane on the page, X to the right, Z down the page and the Y axis out of the page, as shown in Figure 2.2. Voxel dimensions are completely variable in all three directions. Each voxel can be specified to be of a particular material.

DOSXYZnrc has several important and unique features, such as dose component calculations, a wide variety of source configurations and beam reconstruction techniques, correlated sampling, use of CT phantom (conversion of CT data to CT phantom via *ctcreate*), restart capabilities, phase space redistribution, as well as other features as detailed in [47].

The code can use energy spectrum, simplified monoenergetic diverging or parallel beams, *phase space* data generated by a *BEAMnrc* simulation, or a multiple source model.

DOSXYZnrc requires an input file which can be a *phase space* file or other source of particles, and a phantom file. The user can manually specify phantom parameters from within the *DOSXYZnrc* interface. There are a number of input parameters that are significant in the reduction of the simulation calculation time, like electron cutoff energy (*ECUT*), number of histories used, the voxel size and phantom size. These input parameters determine the output of the whole run. At the same time they play a significant role in the duration of the run, and can save important computing time when wisely chosen. The output of the *DOSXYZnrc* is an array of voxels and the dose deposited in each of them [47].

When the global electron cutoff energy (global *ECUT*), an *EGSnrc* input parameter, is smaller than electron cutoff (*ECUT*) or is missing from the input file, the *ECUT* is used as global cutoff energy, which strongly influences the simulation time [47].

Once the total energy of an electron is lower than the cutoff energy *ECUT*, the electron history is terminated, and all its energy is deposited in the present region. A high energy electron can undergo many interactions before it can be ignored. That is why the choice of the *ECUT* is difficult and depends on the type of process to be simulated. In order to ensure that the electron energy is transported and deposited into small voxels correctly, the range of electrons at *ECUT* is usually set to less than 1/3 of the voxel size [48].

Setting up a simulation involves specification of a large number of *DOSXYZnrc* variables and options. Some options and settings are well documented in the user interface help buttons or entries in the electronic manuals. However, other options are less well documented.

The extension of the output file in the *DOSXYZnrc* simulation procedure is *.3ddose* and some interfaces have been made by the NRC group along with the *DOSXYZnrc* to extract and visualize the dose information from the *.3ddose* file. The names of those interfaces are *STATDOSE* and *DOSXYZ_SHOW* [49], respectively.

STATDOSE **interface**

During this research *STATDOSE* user code was used to analyse the dose distribution in the CVD diamond detector as it gives a better visualisation of dose distribution as percentage depth dose (PDD), and profiles.

STATDOSE is an interactive command line interface computer program for 3D dose analysis, and it plots 2D dose distributions using the *Xvgr/Xmgr* plotting package. Its functions include normalization, plotting, and analysis of the dose distributions.

STATDOSE is run from a terminal to extract numerically absorbed dose data from a *.3ddose* file for plotting depth dose curves and beam profiles. The program is used to call the *xmgrace* software to display data as graphs.

The *xmgrace* is an independent software customized on *BEAMnrc* for three dimensional plots. Once a *.3ddose* file is selected, it must be assigned one of the two numbered temporary files, which allows the *.3ddose* files to be compared for analysis. Then data is normalised, plotted and saved in ASCII format. The ASCII file can be retrieved from *xmgrace* plot files or saved files. Dose distributions can be compared statistically and graphically.

DOSXYZ_SHOW **interface**

Dose distribution results simulated with *DOSXYZnrc* can be viewed graphically by using the *DOSXYZ_SHOW* interface [49].

DOSXYZ_SHOW is a graphical visualization interface, which requires the dose distribution *.3ddose* file, as well as the *.egsphant* file containing the phantom geometry, both of which are dose distribution simulation *DOSXYZnrc* output files

(the other four files generated by *DOSXYZnrc* are *.egsinp, .egsdat, .egslst*, and *.errors*).

The *DOSXYZ_SHOW* code is also part of the OMEGA project, and it is used for the representation of the isodose curves of the dose distribution. The code illustrates the density distribution in a specific plane (XY), (XZ) or (YZ) in a grey scale with the corresponding isolines and/or in a colour wash version.

Isodose lines calculation is completed by using linear interpolation between the grid dose points. For simulation efficiency, the isodose lines are approximated with straight line segments from one voxel to the other.

DOSXYZ_SHOW offers the user several options for viewing the geometry: changing the slice, selecting the view plane, zoom in, zoom out, dose normalization, isoline levels, image expansion, point dose values, colour wash representation and density range.

2.4.4 PEGS DATA code

In addition to the previously presented user codes, the *EGS4* package includes *PEGS4*, a code which allows calculation of the cross section data of the media. In *EGSnrc/BEAMnrc* an interface also has been made to execute the *PEGS4* execution file and generate the cross section data which are known as *PEGS* data. In *EGSnrc, BEAMnrc* and *DOSXYZnrc*, any user defined materials/medium can be simulated by using the corresponding *PEGS4* data.

PEGS4 can be used to simulate impurities inside different media, including the synthetic diamond detector. The code can virtually vary the diamond detector material by just changing the type and fraction of the impurities, allowing the researcher to find the best diamond structures for different applications.

Chapter III

Development of a Monte Carlo model

3.1 Introduction

This chapter describes the steps involved in the development of a Monte Carlo model for the simulation of a small (sub-millimeter) size CVD diamond detector with thin electrodes. Investigations of the non-uniform voxels in the uniform voxeled water phantoms for the simulation of very small voxels are outlined, as it is the exploration of the *EGSnrc/DOSXYZnrc* code capacity to simulate small voxels for modelling the diamond detector's components, diamond film and electrodes. Finally, the obtained Monte Carlo model is validated against a model from the literature and experimental results.

3.2 Materials and methods

The Monte Carlo simulations in this project were run using a computer with a dual core Xenon processor of 2.2 GHz speed for each core. The Debian-based Ubuntu 6.06 version operating system and a Fortran g77 compiler were used in the installation of the Monte Carlo code. The Monte Carlo code *EGSnrc* [38] and the user codes *BEAMnrc* and *DOSXYZnrc* were used in this work.

In *EGSnrc/BEAMnrc* and *DOSXYZnrc*, a beam can be modelled in three different ways: from the energy spectrum, from the multiple source model, or from the *phase space* file [42]. Initial investigations to model the CVD detector and its Monte Carlo parameters were done by modelling the beam from the energy spectrum produced by Mohan et al. [50].

The *DOSXYZnrc* code was employed to simulate a water phantom and the CVD diamond detector components (electrodes and diamond layer) and to calculate the dose distribution inside the detector. The water phantom was simulated by using water voxels of the same dimension throughout the phantom, with the exception of the detector (always modelled with voxels smaller than the ones used for the phantom). Simulation of the detector, located at different positions inside the phantom, was achieved by using very small size voxels and different materials for the detector core and the electrodes. The materials used to model the layers of the detector and the water medium were taken from the default list of materials of the *cross section data* files.

The input file for the *DOSXYZnrc* contains information related to the water phantom dimensions, the voxel dimensions used to define the phantom, the CVD diamond detector characteristics (diamond thickness, electrode thickness and composition), and the description of the *source data* file and *EGSnrc* parameters.

The *STATDOSE* code was used to analyze *DOSXYZnrc* dose data *.3ddose* output files. *DOSXYZ_SHOW* displays the density distribution output in a given plane, and shows with grey or colour wash representation the dose distribution and the corresponding isodose lines. *Xvgr/Xmgr* were used for analysis and plotting.

3.2.1 Initial simulations

Figure 3.1 shows the most common diamond radiation detector, in the form of two terminal electronic devices with a metal-insulator-metal (MIM) structure. A high sensitivity diamond is sandwiched between two metal electrodes connected to an external voltage to provide an electric field across the device. Free carriers are generated by the absorbed radiation inside the diamond. These free carriers interact with the electric field generating a current in the external circuit.

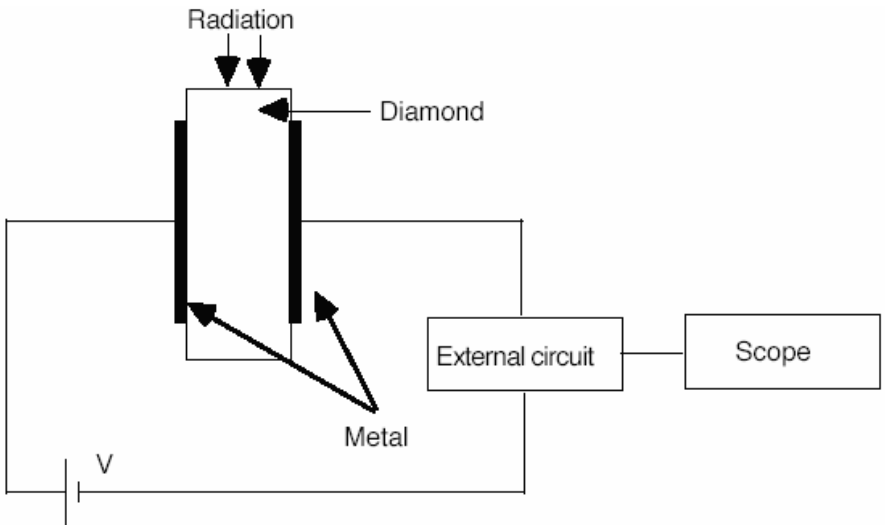

Figure 3.1 Schematic diagram showing a diamond MIM detector, from reference [14]

Initial investigations were related to the water phantom and voxel dimensions in order to facilitate the simulation of a small CVD diamond detector. The modelled CVD detector dimensions and properties are in analogy with a prototype detector being developed by other members of the research group, as shown in Figure 3.2. The experimental set up can be seen in Figure 3.3.

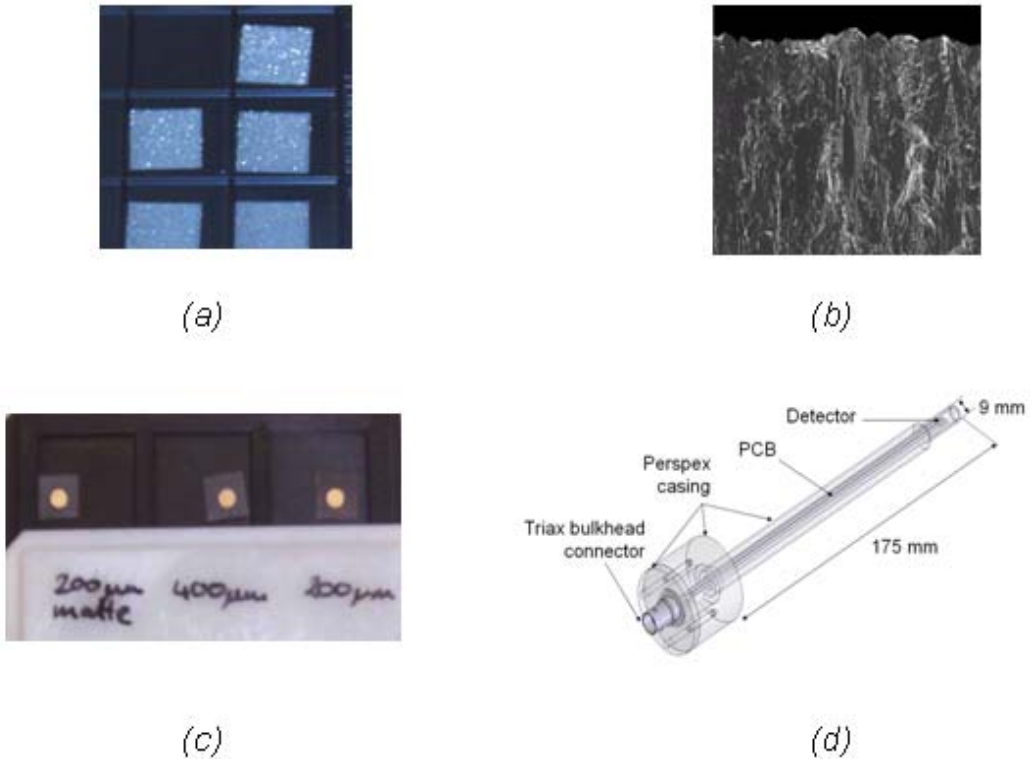

Figure 3.2 a) Samples of the CVD diamond film used at Canterbury University for the design of the CVD diamond detector
b) Side view of the diamond structure
c) Diamond film and electrode configuration used in the construction of the CVD diamond detector for different diamond film thicknesses
d) Prototype of the encased CVD diamond detector [29]

To simulate the real setup situation for a phantom and diamond detector exposed to the photon beam (Figure 3.3), the following initial *DOSXYZnrc* parameters were chosen:

- *cross section data* file *700icru.pegs4*, which is generally recommended for high energy photons and contains the information about the materials used in the simulations;
- *global electron cutoff energy (ECUT)* of 0.7 MeV, which means that if the energy of an electron drops below 0.7 MeV the electron is no longer tracked and its energy is deposited in the current region [42];

- *global photon cutoff energy (PCUT)* of 0.01 MeV, the recommended value, which means that all Bremsstrahlung events are simulated as discrete events [42].

Figure 3.3 Experimental setup of the CVD diamond detector in the water phantom for a 6 MV photon beam

The source type chosen for the initial simulations was *parallel beam from the front* along the Z direction. The beam was modelled from the 6 MV energy spectrum produced by Mohan et al. [50] which is usually stored in the *HEN_HOUSE* directory, the home directory tree of the *EGSnrc* system. In all the simulations, a 10 × 10 cm^2 field size perpendicular to the Z direction (Figure 2.2) was used. The water phantom and the detector materials were created using the *PEGS4* code which allows the calculation of the *cross section data* of the media used in simulations. The material selected to define the phantom was water, and the detector was defined with a carbon core and metal electrodes.

The CVD diamond detector with metal/carbon/metal structure is illustrated in Figure 3.4. The carbon core and the electrodes were modelled as having square shapes, closely approximating the real geometry of the detector.

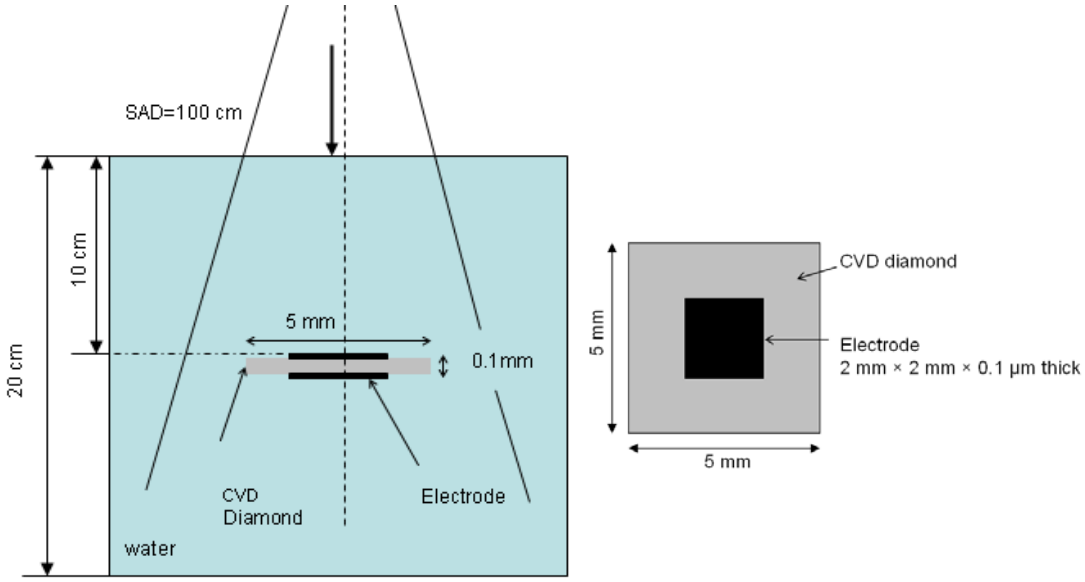

Figure 3.4 a) Illustration of the CVD diamond detector (diamond film and electrodes) at 10 cm depth in the water phantom, and detector's dimensions and orientation in the photon beam
b) Lateral view of the CVD diamond detector showing the metal electrode

Initial simulations were run with all the *EGSnrc* parameters kept as default, with the exception of the *number of histories* which were given different values to obtain a balance between minimising the statistical error and not having an extremely long simulation run time (the larger the *number of histories*, the longer the simulation run becomes, and the lower the statistical error).

3.2.2 Comparison between uniform and non-uniform voxels in water phantom simulations

By using *DOSXYZnrc*, phantom structures can be simulated either with similar voxel sizes (uniform water phantom), or with voxels of different dimensions (non-uniform water phantom). Both are described below as an explanation to why the non-uniform water phantom option was preferred. Note that in this section the composition of each voxel in the different groups was water.

In MC simulations, calculation time and statistical errors depend on the number (implicitely the size) of the voxels. Simulation of the CVD diamond detector with an electrode thickness of 0.1 μm is challenging because of the big differences in the size of the voxels used for the detector, the electrode and the water phantom. The results of each individual simulation include different statistical uncertainties caused by the different dimensions of the voxels used in that simulation. Statistical errors in bigger voxels are less than the errors shown in the very small voxels representing the detector core and the electrodes.

The impact of the different non-uniform voxel sizes of the CVD and electrodes with respect to the voxel size of the water phantom were investigated in this work. Water was considered for all of the different sized voxels as the medium for the transported particle.

Uniform water phantom

At the beginning of the simulations, the water phantom was defined using uniform voxels throughout its entire volume.

The size, and hence number of voxels necessary to define the water phantom depends on the minimum thickness structure that needs to be simulated, in this work the electrodes of the detector. To simulate very thin electrodes, voxels of the required dimension needed to be defined.

The maximum number of voxels that can be simulated using the standard *DOSXYZnrc* code is limited by the default number of voxels for the X, Y, and Z directions (128 × 128 × 56). The number of voxels also depends on the phantom size, thus by decreasing the overall size of the water phantom the number of voxels per unit length can be increased. However, the size of the water phantom is dictated by the size of the radiation field, i.e. the phantom has to be larger than the radiation field. Therefore, one way of increasing the number of uniform voxels to the number that facilitates the simulation of very small electrode thicknesses, would be

to decrease the radiation field size. Due to practical considerations this approach did not suit the requirements for the simulation.

The lowest standard geometry the radiation field could be set to was of 4 × 4 cm^2, and the voxel size could not be reduced enough. For smaller field sizes, the phantom became too small and did not resemble the real setup. Voxels with dimensions in the range of millimeters would be obtained. This size range is much larger than the desired electrode thickness of 0.1 μm.

Another way to increase the maximum number of voxels, in order to enhance the *DOSXYZnrc* code capabilities, is to change the number of voxels in the *DOSXYZnrc* file *dosxyznrc_user_macros.mortran,* and recompile to make the file effective. The number of voxels in the Mortran file was changed from 128 × 128 × 56, to 300 × 300 × 200 for the X, Y and Z directions. By using this file, all the voxels in the 20 × 20 × 20 cm^3 uniform water phantom could be modelled as having a dimension of 0.1 × 0.1 × 0.1 cm^3.

Non-uniform water phantom

In these simulations the same voxel dimension was used for the phantom, while the detector voxel size was changed. The very thin detector electrodes needed to be simulated with voxels of very small dimensions.

As previously explained, results gathered and analyzed at the beginning of the work showed that the standard number of voxels had to be increased. However, the increased number of 300 × 300 × 200 voxels was still not enough to model the whole 20 × 20 × 20 cm^3 water phantom by using only voxels of a thickness of 0.1 mm (the thickness of the CVD detector).

The answer to this problem was the simulation of the phantom and the detector by using different voxel sizes for each of the modelled elements. Each of the

geometrical element of the simulation (the water phantom, the CVD, and the electrode) was modelled as having its own voxel dimension.

In *DOSXYZnrc* voxels can be defined individually or as groups. Attempting to model the water phantom voxel by voxel, with each voxel having a different size proved to be a much too laborious alternative because of the very small voxel insertions for the detector structure, and implicitly the large number of voxels involved in the definition of all the simulated elements.

The optimum solution, both from a simulation time point of view, as well as the precision of the results, proved to be groups of voxels with different sizes for the detector film, electrodes and the phantom itself.

Comparison between absorbed dose distributions for uniform and non-uniform voxels in water phantoms gives information about the dose variation in a specific voxel and consequently contributes to the improvement of the water phantom definition for further simulations related to the CVD diamond detector.

In the first part, a simulation was done for the uniform phantom. *DOSXZYZnrc* was used to simulate a 20 × 20 × 20 cm^3 uniform water phantom with a unique voxel size of 1.0 × 1.0 × 0.1 cm^3. The phantom was defined using 200 voxels along the Z direction and 20 voxels for each of the X and Y directions. A radiation field size of 10 × 10 cm^2 for a 6 MV photon beam was modelled to irradiate the water phantom using the Mohan energy spectrum stored in the *Hen-House* directory of *EGSnrc/BEAMnrc* tree structure.

The results from this simulation were compared with the dose calculated for a non-uniform water phantom with the same overall size (20 × 20 × 20 cm^3). A voxel size of 1.0 × 1.0 × 0.1 cm^3 was used for the water phantom, with the exception of five central voxels representing the detector. The detector orientation was perpendicular to the beam direction, and the whole setup was irradiated for the same field size of

10 × 10 cm^2. Several non-uniform voxels in the water phantom simulations were done, including detectors of different geometries, as detailed below.

First, the geometry of the detector was simulated employing water voxels (voxels having the selected material as being water, not metal or carbon) with a 1/3/1 μm (electrode/diamond/electrode) thicknesses, located at a depth of 10 cm, perpendicular to the direction of the beam, as shown in Figure 3.5. Water was selected as the material for the detector in order to eliminate the influence of the detector material on the absorbed dose.

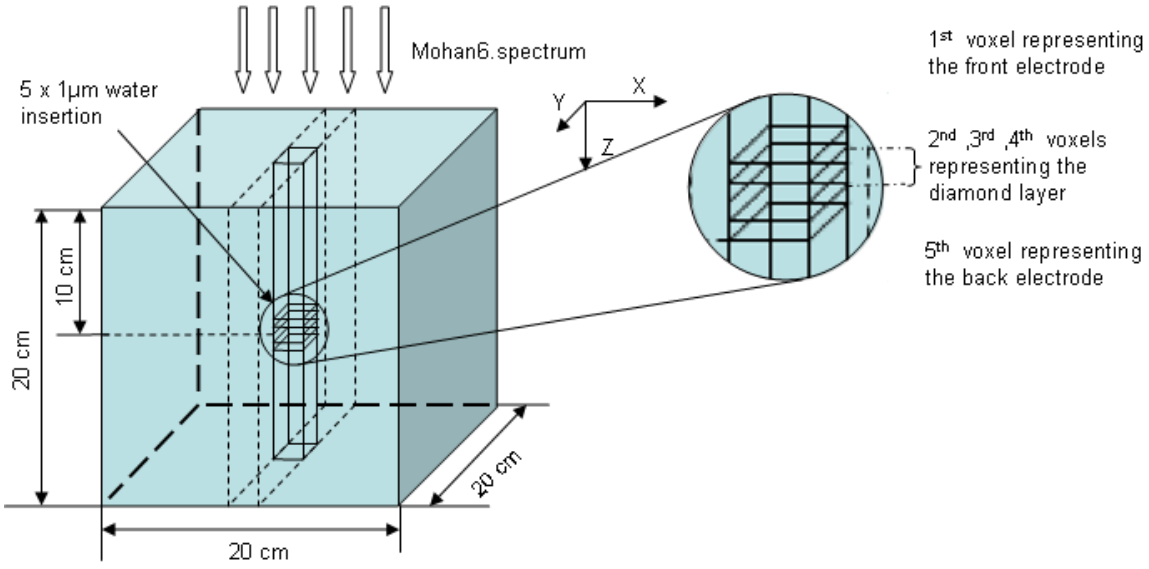

Figure 3.5 Schematic diagram showing the detector geometry and water voxels insertion at 10 cm depth in a 20 × 20 × 20 cm^3 water phantom for a single photon beam with *Mohan6.spectrum*

Next, simulations were carried out to analyze the influence of the detector geometry on the dose readings. The physical dimensions of the detector were varied to reach an optimum shape.

Modification of the detector geometry and structure was done as follows:

- The detector was modelled in a sandwich like structure keeping the same thickness $X_e = X_d = 1$ µm for the electrodes and the diamond, but changing the length and width of the electrode. The three layers of the detector were modelled as having the same dimensions (length, width and thickness), as shown in Figure 3.6a.
- Next, the three detector layers were combined, and the structure was modified to a simpler one, by considering the whole detector as having one layer only (Figure 3.6b).
- Finally as shown in Figure 3.6c, the single layer of the detector structure was modelled at different thicknesses, of $X_d = 1$, 5, 9, 10 and 100 µm.

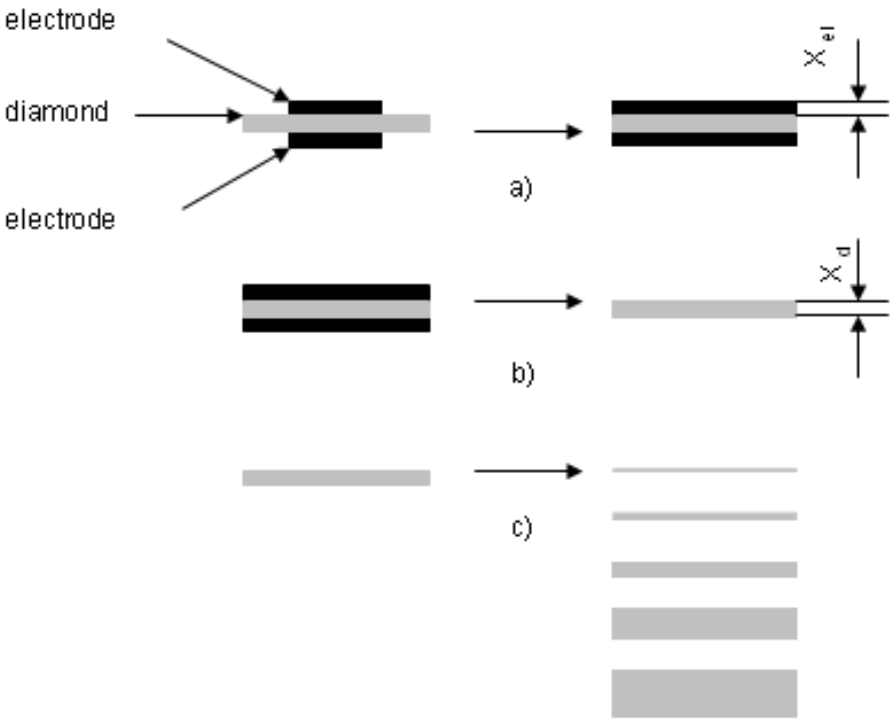

Figure 3.6 Detector steps for the simplified structure
a) Sandwich design structure
b) One layer detector structure
c) Different detector thicknesses

The absorbed dose was simulated for all the described geometries. A similar setup (water phantom, beam orientation, source file and field size) was used for all these simulations. The *number of histories* in *DOSXYZnrc* was set to 100 million, with the *EGSnrc* parameters options as default for high energy photon beams. The results were compared with the dose from the uniform water phantom at the level of detector insertion.

It was found that variation of the detector dimensions strongly influenced the dose. The next section describes how the Monte Carlo parameters were adjusted to address this issue. For results see section 3.3.

3.2.3 Determination of the Monte Carlo parameters

Thin detector geometries lead to high dose variations, with a peak forming at the location of the detector. The choice of the *EGSnrc* MC parameters needed careful exploration for a better understanding of the "beam distortion" through the smaller inserted central voxels. Therefore, several *EGSnrc* parameter combinations were investigated. The studied parameters were the *cross section data* file, the *boundary crossing algorithm (BCA)*, and the *HOWFARLESS* option.

The *700icru.pegs4* file is recommended for high energy photon simulations. In all the initial simulations this *cross section data* file was used, as the aim was to simulate a high energy 6 MV photon beam. Investigations using the cross section data *700icru.pegs4* and *521icru.pegs4* were undertaken to understand their appropriateness to calculate doses in a small voxel.

The *boundary crossing algorithm* is one of the parameters characterizing the transport of radiation through the material. *PRESTA-I* is the default option of the algorithm, and is used for efficiency reasons to shorten the iteration time. To improve precision, the *EXACT* option of the algorithm can be used. The *EXACT* option requires longer simulation times.

The simulations made for the comparison of the uniform and non-uniform voxels in water phantoms were run using the *PRESTA-I* default option of the *BCA*. This means that the lateral path length corrections were switched off if the perpendicular distance from the electron to the boundary became less than the distance given by the *skin depth* option in the *boundary crossing algorithm* (s*kin depth for BCA* option). Once the electron reaches the boundary, a multiple scattering event is forced.

The *EXACT* option of the *BCA* is recommended in simulations where charged particle equilibrium can not be reached (with the *PRESTA-I* default option) or when there is a "large difference in size between dose voxels and voxels making up the rest of the phantom" [42]. The *EXACT* algorithm will go into single scattering mode as soon as the electrons are within a certain distance from the boundary, distance given by the *EGSnrc* input *skin depth for BCA,* as previously explained.

The *HOWFARLESS* algorithm can be used to increase the efficiency of dose calculations in a homogeneous phantom. The parameter is recommended to be "off" (the default setting) in all homogeneous phantom calculations. This allows the dose to be calculated inside each of the phantom voxels. The "off" default setting of the *HOWFARLESS* option was used for the uniform and the non-uniform voxeled phantom simulations mentioned above.

When the *HOWFARLESS* option is "on", the *HOWFAR* and *HOWNEAR* subroutines in *DOSXYZnrc* only consider the extreme outer boundaries of the phantom. The algorithm efficiency depends on the source type, energy, field size, phantom voxel size, and the *boundary crossing algorithm* used [42].

To find the optimal Monte Carlo parameters, eight simulations were performed using the *EGSnrc* parameter combinations shown in Table 3.1.

In simulations where the *700icru.pegs4* data file was used*, ECUT* was 0.7 MeV and *PCUT* 0.01 MeV, while in simulations using the *521icru.pegs4* data file, the *ECUT* was 0.521 MeV and *PCUT* 0.01 MeV.

These simulations were the basis for all further work in this research. Based on the results which are discussed in detail in section 3.2, in all the rest of the simulations combination number 8 shown in Table 3.1 was selected (*521icru.pegs4*, *EXACT BCA*, and *HOWFARLESS* "off"), which showed minimum dose deviations in the region of the detector voxels insertion.

Table 3.1 *EGSnrc* transport parameter combinations used for the absorbed dose analysis for the small water voxel size

MC parameter combination	***Cross section data* file**	***Boundary crossing algorithm***	***HOWFARLESS algorithm***	***Number of histories*** (million)	**All other *EGSnrc* transport parameters**
1	*700icru.pegs4*	*PRESTA-I*	*on*	100	Default transport options
2	*700icru.pegs4*	*PRESTA-I*	*off*	100	Default transport options
3	*700icru.pegs4*	*EXACT*	*on*	100	Default transport options
4	*700icru.pegs4*	*EXACT*	*off*	100	Default transport options
5	*521icru.pegs4*	*PRESTA-I*	*on*	100	Default transport options
6	*521icru.pegs4*	*PRESTA-I*	*off*	100	Default transport options
7	*521icru.pegs4*	*EXACT*	*on*	100	Default transport options
8	*521icru.pegs4*	*EXACT*	*off*	100	Default transport options

3.2.4 Benchmarking of the Monte Carlo model

Confirmation that these *EGSnrc* Monte Carlo parameters would yield sensible results, required validation of the modelling strategy. In this section two validations were done. One was to reproduce the published results for a specific setup, and the other one was to verify the accuracy of the dose calculation by *DOSXYZnrc* for the MC setup by comparing simulation results with experimental data.

Comparison with published results

Minimization of the dose deviations through the detector was the reason for considering the use of the *EGSnrc* transport parameter combination *521icru.pegs4, EXACT BCA*, with *HOWFARLESS* "off".

Work published by Gorka et al. [27] was used to validate the chosen input parameters. In his work, Gorka used a different Monte Carlo code, *PENELOPE*, to study the photon energy deposition in a CVD diamond detector. The Monte Carlo simulations in his study were focused on the metal/diamond interface phenomena in a semi-infinite planar geometry. An illustration of Gorka's simulation setup is shown in Figure 3.7a.

Similar to the studies by Gorka, the simulations in this research investigated the absorbed dose distribution in the diamond layer of the CVD diamond detector. Comparison of the setup used by Gorka and the model employed in this work is shown in Figure 3.7.

It can be seen that the setups are comparable, with the exception of the phantom's depth on the Z direction (10 cm in Gorka's work, 30 cm in this research). The water phantom dimensions of 30 × 30 × 30 cm^3 were chosen for a better simulation of the real setup geometry. The different phantom depths are not of an issue given that in

both simulations the diamond detectors are located at the same depth inside the phantom, where the interest zone (for dose distribution comparison) is.

Gorka's semi-infinite slab geometry consisted of diamond layers of different thicknesses from 50 μm to 0.2 cm and two silver electrodes with thickness of 0.07 cm each, one on each side of the diamond layer. A 1.25 MeV monoenergetic photon pencil beam was applied perpendicular to the detector.

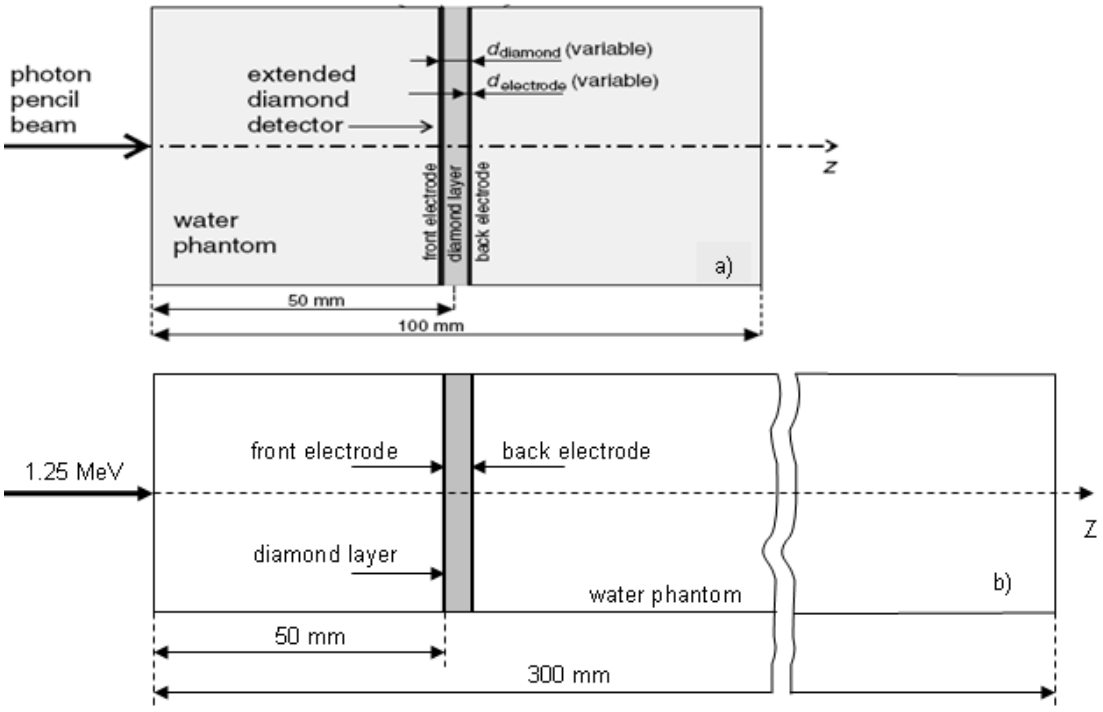

Figure 3.7 a) Geometry of semi-infinite slabs used by Gorka et al.: a diamond layer with electrodes on both sides, taken from reference [27]
b) Geometry of the setup used in this research

For validation, the CVD diamond detector in this work was modelled in the same silver/carbon/silver structure with 0.07/0.2/0.07 cm thickness respectively. The diamond layer was created using the *PEGS4* user code to generate the CVD with a density of 3.51 g/cm^3, which was added to the *521icru.pegs4* materials list. A monoenergetic beam of Cobalt 60 mean energy 1.25 MeV along the Z direction was considered in the simulation. The absorbed dose in the detector and the surrounding water phantom was analyzed using the *STATDOSE* code.

Verification of dose calculations for the MC setup

As mentioned before, the beam can be modelled from the energy spectrum, the multiple source model, or from the *phase space* file. A comparison of PDDs calculated from the energy spectrum and the *phase space* file was done to investigate their difference in dose calculations. Since all of the investigations in this chapter were done by modelling a beam from the 6 MV energy spectrum calculated by Mohan et al. [50], this comparision lead to finding the appropriate procedure for the modelling of the beam. The absorbed dose through the simulated phantom was compared with the data commissioned from a 6 MV photon beam generated by a Varian 2100C linear accelerator.

A uniform 30 × 30 × 30 cm^3 water phantom with a 10 × 10 cm^2 radiation field was simulated using the *Mohan6.spectrum* energy file for the generation of the beam.

Experimental measurements were done using a waterproof 0.1 cm^3 RK ion chamber (Scanditronix) with interior radius of 2 mm and the polarization voltage of 250 V. The chamber measured the radiation dose at depths of 0 to 50 cm inside a water tank.

3.3 Results and discussion

3.3.1 Initial simulations

The CVD diamond detector manufactured by chemical deposition includes extremely thin deposited layers, with electrodes of 0.1 μm thick. Initial simulations for the uniform water phantom showed that the detector could not be modelled with 0.1 μm thin electrodes, because of the limited number of voxels in *DOSXYZnrc*. Therefore it had to be simulated at a bigger scale. Preliminary trials were done

starting with a detector using aluminium as material for the electrode and carbon for the detector core, each with thicknesses of 0.4 cm (see Figure 3.8).

Further on, the detector layer thicknesses were reduced down, to reach minimum values of 1 μm for the electrodes in the final set of experiments. This will be shown later in the determination of the Monte Carlo parameters.

The uniform water phantom was investigated for different dimensions and different voxel sizes in order to obtain the simulation of a very small voxel. As mentioned in sub-section 3.1.2, the water phantom dimension can not be decreased more than the radiation field size, and the maximum number of voxels in all directions is limited by the preset number of the *DOSXYZnrc* code. This limitation was overcome by changing the preset number of voxels in the Mortran file of the code.

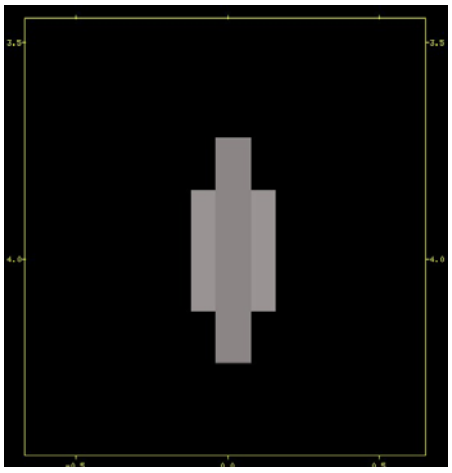

Figure 3.8 Initial simulation of the detector, using the default MC parameters of the *EGSnrc* code

It was observed that DOSXYZ_*SHOW* code can not display structures containing different size voxels. They are displayed by the code as having the same voxel dimension. This was verified by doing one simulation that included three successive carbon slabs with different thicknesses (0.01, 0.001, 0.0001 cm), separated by water voxels of identical sizes. The simulation was done by using dissimilar voxel groups inside the phantom. *DOSXYZ_SHOW* considered the size of the first group of

voxels (situated at the edge of the phantom) as default, and displayed all (water and carbon) voxels as having the same thickness. Due to this limitation, *STATDOSE* code was used for proper analysis of the dose throughout the phantom and the detector. The use of the *STATDOSE* code allowed the results to be shown as graphs of relative dose with depth.

3.3.2 Comparison between uniform and non-uniform voxels in water phantom simulations

Inconclusive results in the initial simulations with default Monte Carlo parameters required planning of further investigations, to see how the very high deviation in dose at detector level could be reduced.

Investigation of the absorbed dose deviation in a very small voxel using the default *EGSnrc* input parameters was accomplished in parallel simulations. The same size of voxels was used for the phantoms as a whole, with reduced size central voxels at the location of the detector for the non-uniform phantoms.

Relative value of the absorbed dose as a function of phantom depth for the uniform and non-uniform voxels in the water phantom are shown in Figures 3.9a-b. Figure 3.9b shows the effect of five identical water voxels of 1 cm × 1 cm × 1 μm, in the phantom, at a depth of 10 cm.

The relative value of the absorbed dose at the insertion level produced a peak of 2.0 over the normal level of 0.75 determined from the uniform phantom, for a history number of 100 million.

Further on, for the detector modelled with five water voxels (one for each electrode, and three for the diamond layer), a total of five non-uniform phantom simulations were done. The aim was to study the nature of the absorbed dose deviation at the level of insertion.

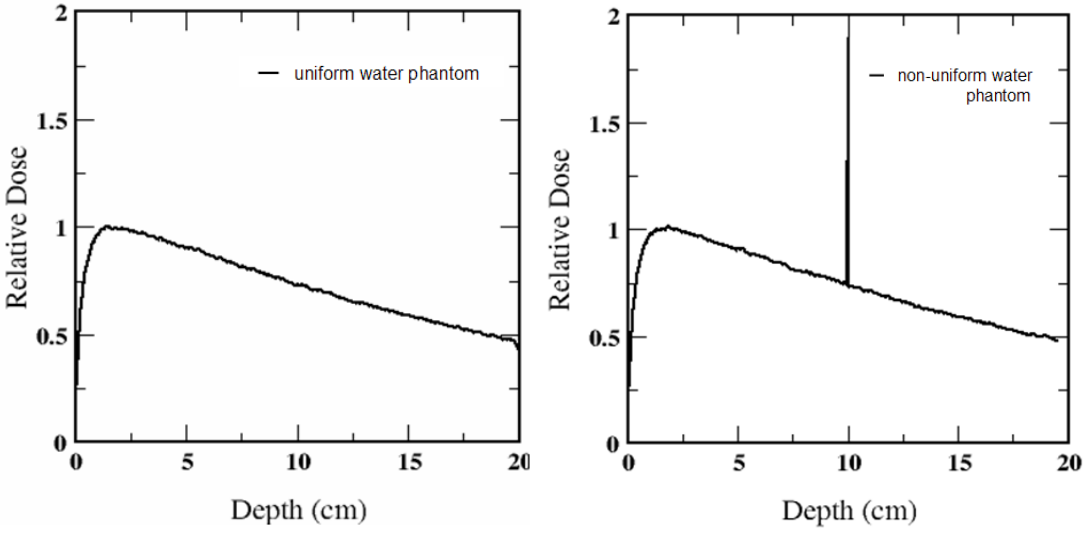

a) b)

Figure 3.9 a) Relative dose in a uniform water phantom
b) Relative dose in a water phantom with five small water voxels inserted at 10 cm depth

The five inserted voxels were positioned perpendicular to the Z direction of the beam, therefore the dimension simulated along this direction was the voxels' thickness. The combined results of the first three simulations with voxel dimensions of 1 cm × 1 cm × 1 μm, 1 cm × 1 cm × 10 μm, and 1 cm × 1 cm × 100 μm are shown in Figure 3.10.

It was found that the thinner the five inserted voxels were, the more the dose deviation increased. The dose measured through the largest five voxels, each of 1 cm × 1 cm × 100 μm (Figure 3.10, green) was very close to the dose measured through the water phantom. For a ten times decrease in the thickness of the voxels, from voxels of 1 cm × 1 cm × 100 μm to voxels of 1 cm × 1 cm × 10 μm, an increase in the absorbed dose, of 12%, was observed (Figure 3.10, red).

Because a very small voxel thickness is required for precise modelling of the CVD diamond detector, the thickness was further reduced ten times from voxels of 1 cm × 1 cm × 10 μm to 1 cm × 1 cm × 1 μm. A 166% sharp increase in the absorbed

dose was observed when compared with the absorbed dose in the uniform water phantom at the same level.

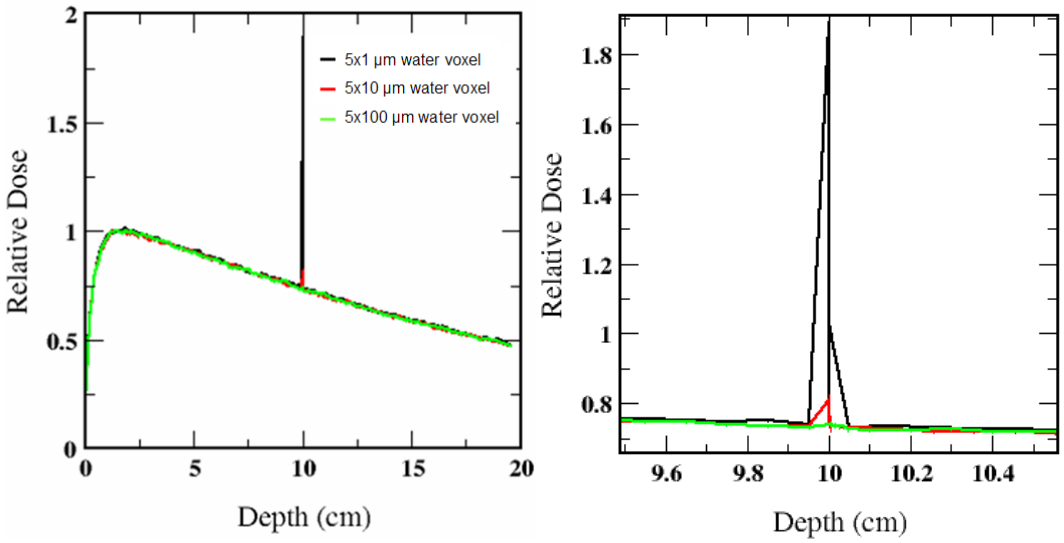

a) b)

Figure 3.10 a) Relative dose variation for different central voxel thicknesses, of 1 µm, 10 µm, and 100 µm
b) Magnification of the region of interest

To see if the peak variation for a certain number of histories depends on the voxel size, when all the other parameters are kept the same, two more simulations were done with voxel size insertions of 1 cm × 1 cm × 5 µm and 1 cm × 1 cm × 9 µm. The two combined results are shown in Figure 3.11. As expected from the previous three simulations, the more the voxel thickness was increased, the lower the deviation became.

The geometry of the detector was further simplified from five voxels, to one voxel of 1 cm × 1 cm × 1 µm. The results obtained from the simulation of the uniform and non-uniform phantoms were compared and analyzed as shown in Figure 3.12. The relative doses obtained from the simulation of the uniform water phantom and the non-uniform water phantom matched well, apart from the section where the very small voxel representing the detector structure was inserted. The non-uniform water phantom showed a 205% dose distortion above the relative dose at the level of the water voxel insertion, of 0.75.

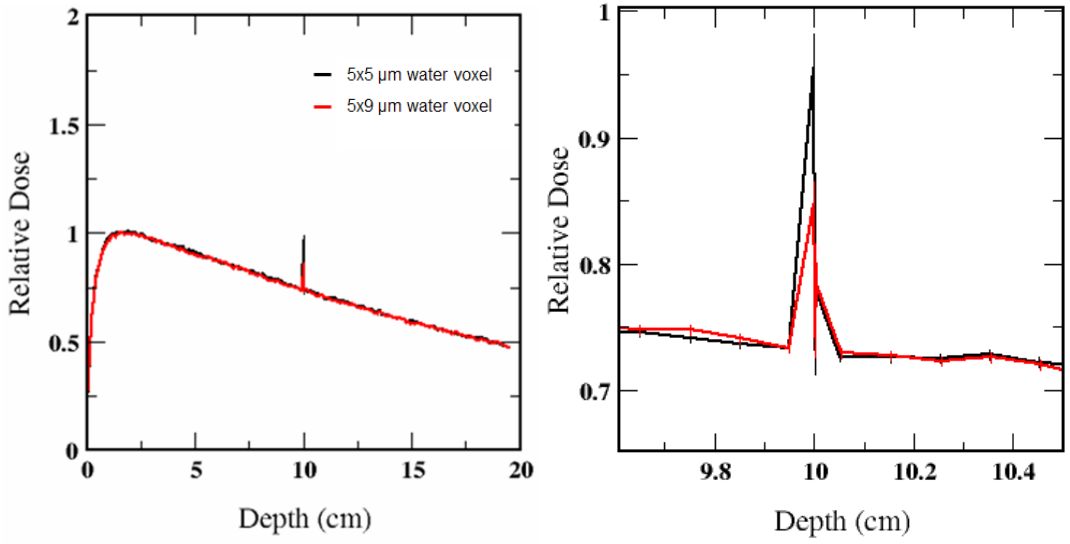

a) b)

Figure 3.11 a) Relative dose variation for different central voxel thicknesses, of 5 µm and 9 µm
b) Magnification of the region of interest

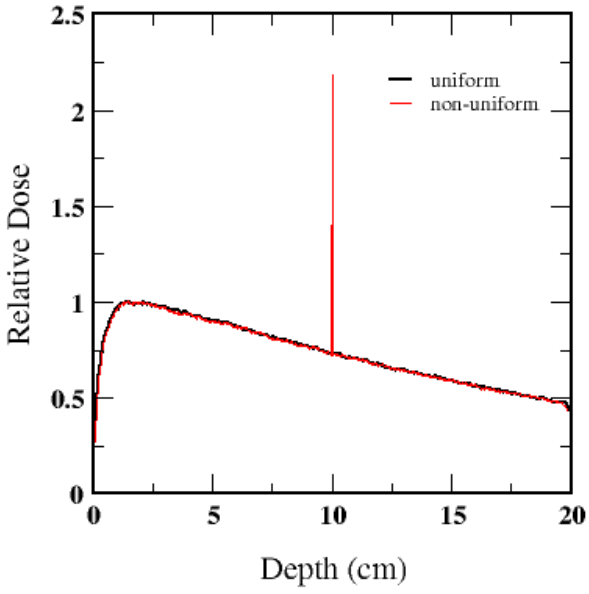

Figure 3.12 Comparison between uniform and non-uniform water phantom for the detector modelled with one water voxel only

Deviation of the absorbed dose at the level of the detector is dependent on the dimension of the inserted voxel since the phantom dimensions, setup geometry and all other Monte Carlo parameters used in the input file were kept identical.

The peak variation for a certain number of histories depends only on the voxel size. Figures 3.10 to 3.12 show that for the same number of histories, a small voxel gives higher peak and relative high statistical uncertainties with respect to the larger voxels. In a phantom with non-uniform voxels, which includes a combination of different size voxels for the water, detector core and electrodes, statistical uncertainty is different for the same number of histories.

3.3.3 Determination of the Monte Carlo parameters

In order not to increase the number of histories to an impractical level, three *EGSnrc* Monte Carlo parameters were studied to investigate their influence on the absorbed dose at the level of the smallest voxel. The parameters were the *electron cutoff energy*, the *boundary crossing algorithm*, and the *HOWFARLESS* option, presented in Table 3.1.

a) Comparison of the absorbed dose in a small voxel using combinations 1, 2, 3 and 4 shown in the table (for the *700icru.pegs4 cross section data*) is illustrated in Figure 3.13.

For the combination of the *PRESTA-I boundary crossing algorithm*, with the *HOWFARLESS* option “off”, the relative value of the dose at the level of the detector was of 2.55, which is 220% higher than the dose measured in the uniform water phantom.

Identical dose values were obtained for both the *EXACT/*PRESTA-*I boundary crossing algorithms*, with the *HOWFARLESS* option “on” (red and blue). The difference between the dose in both these simulations and the dose measured in the uniform phantom was of 11%.

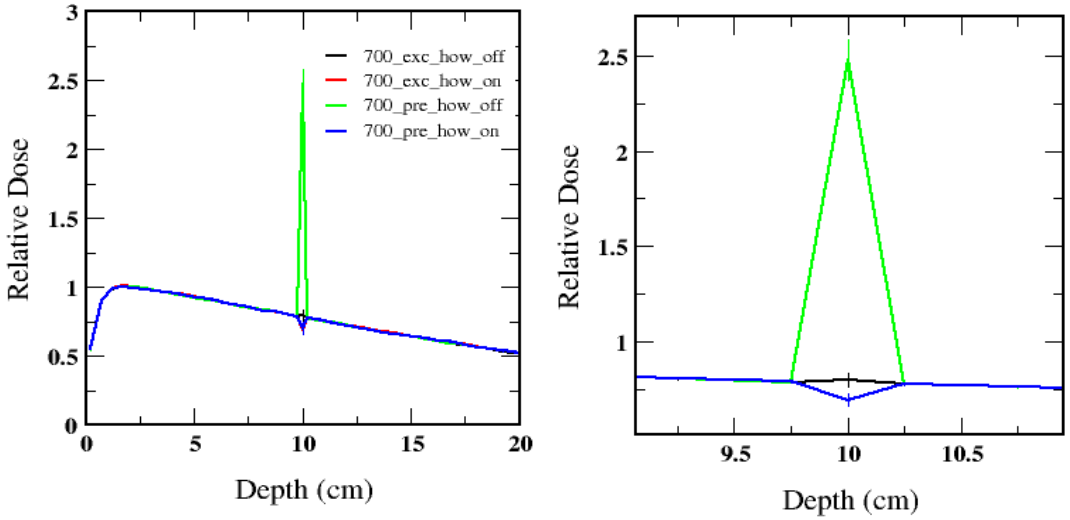

a) b)

Figure 3.13 a) Investigation of the *700icru.pegs4 cross section data* for *EXACT/PRESTA-I boundary crossing algorithm* and *HOWFARLESS* option "on" / "off"

b) Magnification of the region of interest

In comparison with the simulations in which the default *EGSnrc* parameters were used, the investigation of the *700icru.pegs4 cross section data* file showed that optimum combination of the *boundary crossing algorithm* and of the *HOWFARLESS* parameter can lead to a significant reduction in the absorbed dose variation at the level of the very small voxel.

b) Variation of the absorbed dose inside the thin detector voxel using the three parameters combined as shown in simulations 5, 6, 7 and 8 from Table 3.1 (for the *521icru.pegs4 cross section data*), is illustrated in Figure 3.14. The magnified graph shows the peak of the dose variation in each simulation.

The largest variation of the dose in the detector area was observed for the combination of the *PRESTA-I boundary crossing algorithm* with the *HOWFARLESS* option "on" (blue). The difference between the dose in this simulation, and the dose from the uniform phantom was of 7%.

Using the *PRESTA-I boundary crossing algorithm* with the *HOWFARLESS* option "off" the difference in dose between the uniform and the non-uniform water phantoms was 6% (green).

Compared to the measurements done in the uniform water phantom, a 5% lower dose was observed for the selection of the *EXACT boundary crossing algorithm* and the *HOWFARLESS* option "on" (red).

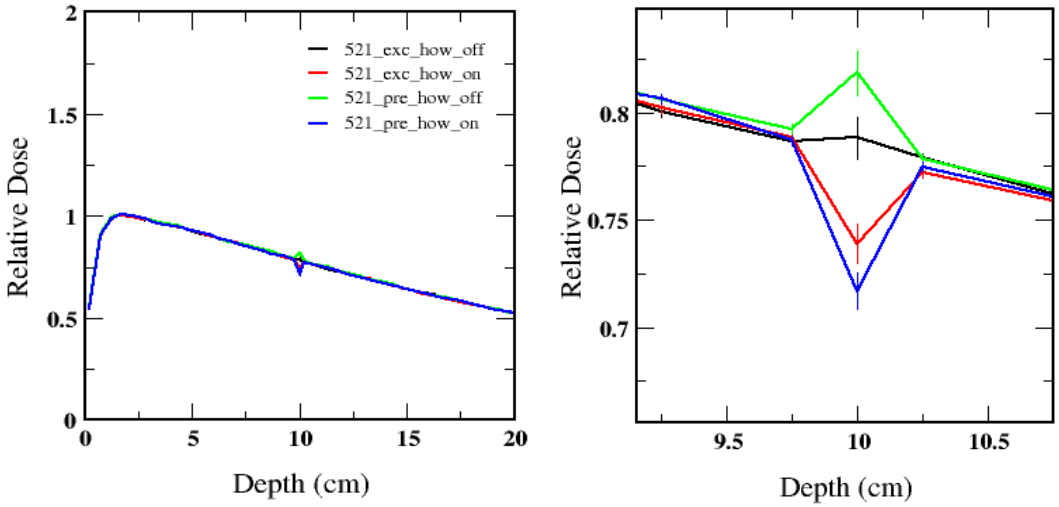

a) b)

Figure 3.14 a) Investigation of the *521icru.pegs4 cross section data* for *EXACT/PRESTA-I boundary crossing algorithm* and *HOWFARLESS* option "on" / "off"

b) Magnification of the region of interest

The dose closest to the one measured in the uniform phantom was obtained by using the *EXACT boundary crossing algorithm* with the *HOWFARLESS* option "off" (black). The difference between the non-uniform and uniform phantom doses was of only 2%.

When reading the percentage values of the differences between the peak doses in the detector and in the uniform phantom, it becomes obvious that the better choice in regards to the *cross section data* is the *521icru.pegs4* option. Comparison

between the results in the two *cross section data* scenarios is done in sub-section c, below.

c) Absorbed dose comparison between *700icru.pegs4* and *521icru.pegs4 cross section data* files, using the *EXACT boundary crossing algorithm* with the *HOWFARLESS* option switched "off" (combinations 4 and 8 in Table 3.1) is illustrated in Figure 3.15.

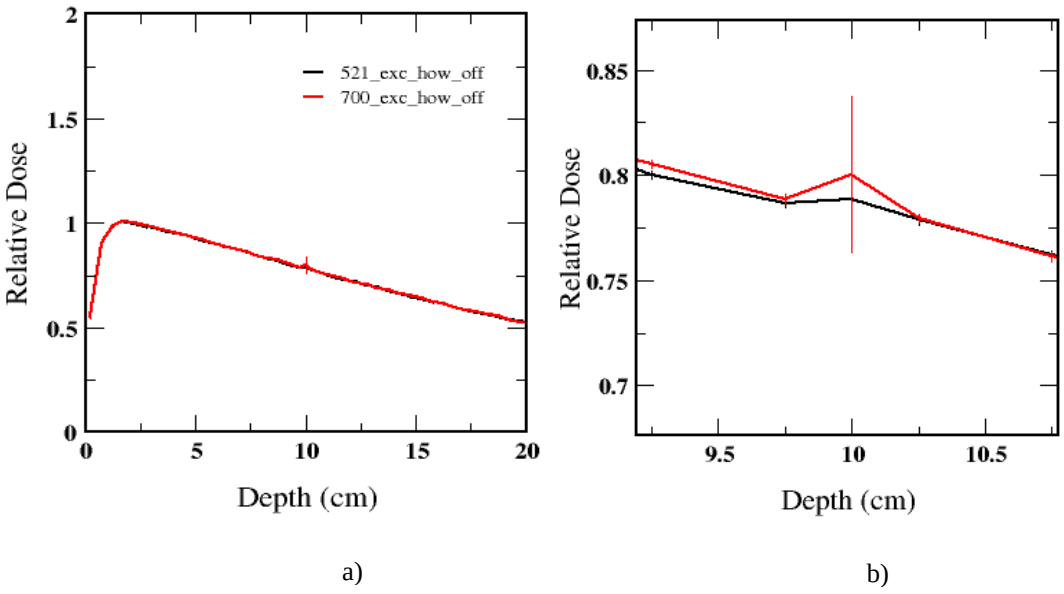

Figure 3.15 a) Comparison of the *700icru.pegs4* and *521icru.pegs4 cross section data*, *EXACT boundary crossing algorithm* and *HOWFARLESS* option "off"
b) Magnification of the region of interest

Figure 3.15b shows the smallest absorbed dose deviations obtained with the *700icru.pegs4 cross section data* and the *521icru.pegs4 cross section data* in the water voxel insertion of 1 μm thick.

The magnified graph illustrates that the smaller absorbed dose deviation in the inserted voxel is achieved for the *521icru.pegs4 cross section data* file.

In Figure 3.15, the use of *700icru.pegs4* high energy cross section data gave a 2% higher dose with higher statistical errors with repect to the use of *521icru.pegs4* low

energy *cross section data*. Low energy photons generated by using the *521icru.pegs4 cross section data* lead to improvement of the statistical error in the small voxel. The *700icru.pegs4* data were generated for the electron total energy of 0.7 MeV, therefore the electrons which have the total energy below 0.7 MeV, will not contribute to the dose deposition procedure. The electron kinetic energy threshold for *521icru.pegs4* data is lower than the threshold for the *700icru.pegs4* data. The use of the 5*21icru.pegs4 cross section data* improves statistical uncertainty for the low energy particle in a small voxel.

These results are in agreement with the user manual of the Monte Carlo code, which indicates that the *PRESTA-I boundary crossing algorithm* can over-estimate the dose in the voxels that are much smaller than the voxels which make-up the rest of the phantom. In these situations the *EXACT boundary crossing algorithm* gives more accurate results. "The *HOWFARLESS* algorithm is used to increase the efficiency of the dose calculations in homogeneous phantoms" [47] by taking into account the extreme outer boundaries of the phantom. The "off" option of the *HOWFARLESS* algorithm increases the calculation time. However, this option allows accurate dose calculations to be made inside each of the phantom voxels.

Therefore, the chosen *EGSnrc* input Monte Carlo parameters used henceforth in all further simulations were the *521icru.pegs4 cross section data,* with the *EXACT boundary crossing algorithm* and the *HOWFARLESS* option turned "off".

3.3.4 Benchmarking of the Monte Carlo model

Comparison with published results

The results from the simulations presented so far, were used as guidance towards the selection of optimum Monte Carlo parameters for accurate dose measurements inside the diamond detector. However, validation of the simulation strategy was required to make sure that further simulations in this work would generate reasonable results. To accomplish this, the *EGSnrc/DOSXYZnrc* MC code was

used to model the CVD diamond detector dimensions and setup conditions, in order to reproduce simulations by Gorka et al. [27]. Similar to Gorka's simulations, the detector was modelled with a 0.2 cm carbon thickness and two silver electrodes, each 0.07 cm thick. The detector was orientated perpendicular to a 1.25 MeV monoenergetic photon beam, as shown in Figure 3.7.

Figure 3.16 shows the dose variation in the CVD diamond detector simulated at a depth of 5 cm, in a 30 × 30 × 30 cm^3 water phantom, with the parameters determined in sub-section 3.3.3.

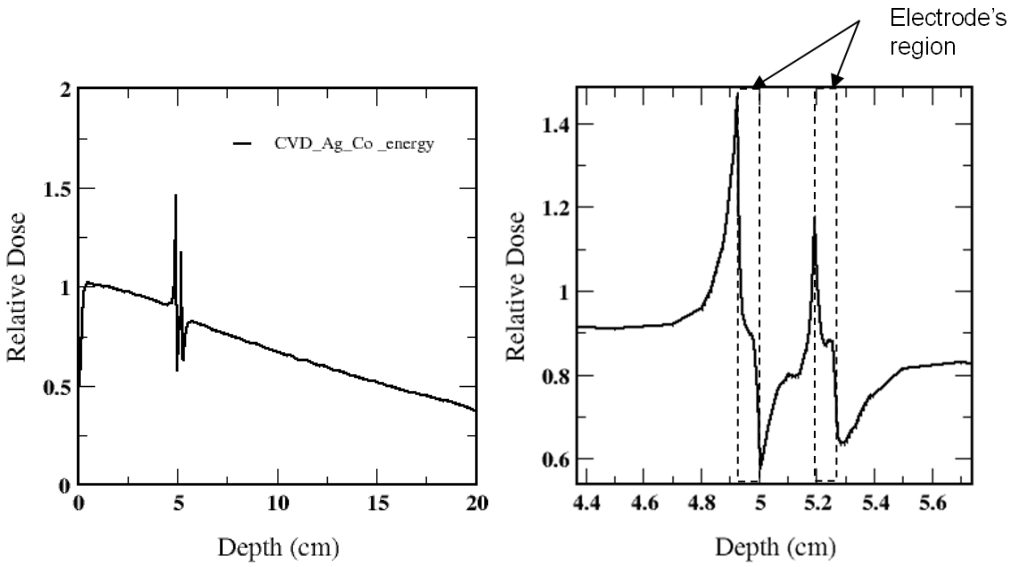

Figure 3.16 a) Relative dose in the CVD diamond detector at a 5 cm depth inside the water phantom for a 1.25 MeV photon beam
b) Magnification of the region of interest

The figure shows high variations in the absorbed dose at the CVD diamond detector level. This is clearly illustrated in the enlarged graph showing the region of interest. The variations are the result of the interface phenomena between high and low atomic number materials. The interface phenomena emerge when the photon beam crosses the detector through its three different layers (silver electrode/ carbon core/ silver electrode).

A sharp increase in the absorbed dose can be observed when the photon beam reaches the first electrode. The dose abruptly decreases while the beam crosses the silver electrode, just to increase again when passing through the carbon layer. Finally, the absorbed dose drops while penetrating the second electrode.

The steep dose increase, observed before the first electrode, is the result of back scatter from the high atomic number (Z = 47) for silver. The radiation is then absorbed into the electrode, decreasing significantly as the photon beam passes through. Once the carbon layer is reached, the absorbed dose increases again as a result of back scatter, till it reaches the second electrode. While passing through this electrode, the dose once more sharply decreases due to its absorption into the electrode material.

The validation was accomplished by comparing this dose variation through the detector simulated in this work using the *EGSnrc* Monte Carlo code, with Gorka's results achieved by making use of the *PENELOPE* Monte Carlo code. Comparison of the results is shown in Figure 3.17.

It can be seen that the relative absorbed dose through the CVD diamond detector has the same trend and magnitude in both Monte Carlo simulations.

The result validates the use of the *EGSnrc* input parameters selected as shown in section 3.3.3. This combination (*521icru.pegs4 cross section data, EXACT boundary crossing algorithm*, *HOWFARLESS* option "off") was therefore used in further simulations to validate the input parameters by using commissioned data.

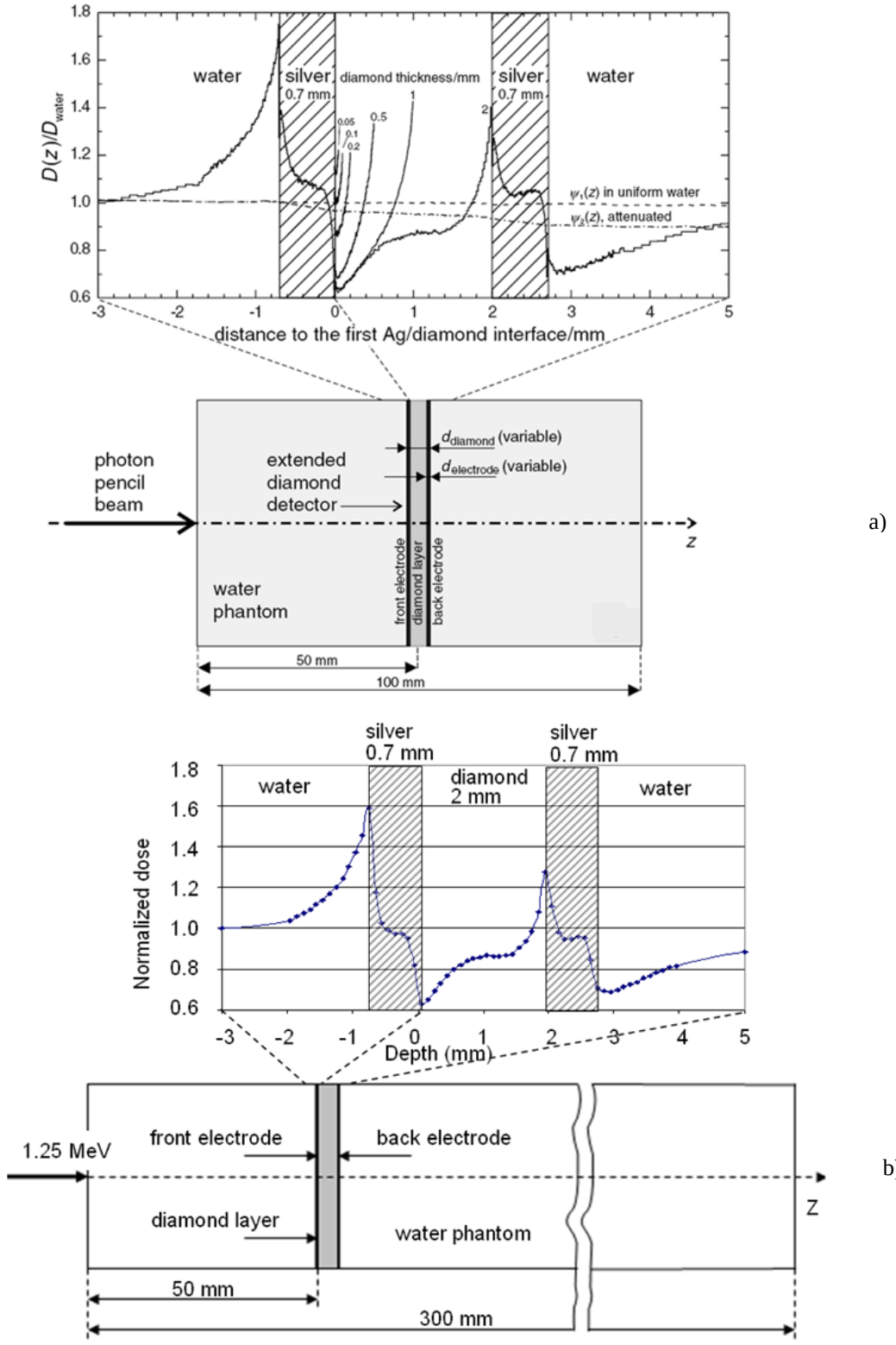

Figure 3.17 Relative value of absorbed dose distribution in a CVD diamond detector
a) Obtained by Gorka et al., using the *PENELOPE* Monte Carlo code [27]
b) Obtained during this work, using the *EGSnrc* Monte Carlo code

Verification of dose calculations for the MC setup

The setup of the Monte Carlo simulations in a uniform phantom needs to validate against the experimental data, therefore the PDDs from two simulations, where beams were modelled from energy spectrum and the *phase space* file, were compared with commissioned data of same energy.

In the first simulation, the beam was defined by using the *Mohan6.spectrum* file. As shown in Figure 3.18, absorbed dose values of the simulated beam (represented by the green curve inside the graph) were much higher than the ones found using the real setup (symbolized by the black curve) for most of the depths of interest.

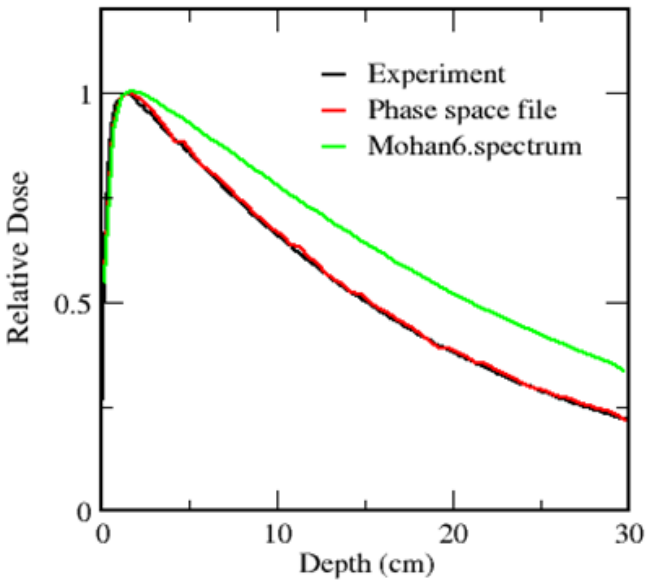

Figure 3.18 Comparison between experimental and simulated dose obtained by using *Mohan6.spectrum* file, and the *phase space* data file as the source file in the *EGSnrc* Monte Carlo simulations

The second simulation was done for the same setup and simulation parameters, with the exception of the energy source generation file which was changed from the *Mohan6.spectrum* to the appropriate *phase space data* files obtained from in-house linear accelerator beams simulated with the *BEAMnrc* code [42]. It was found that

the dose curve from this simulation (the red curve) closely matched the experimental data.

This final result confirmed that beams modelled with the *phase space data* file generate much more appropriate simulations than simulations with beams generated using the *Mohan6.spectrum* file. Therefore all the simulations that follow were done using the *phase space* data file for beam source modelling.

It should be noted that optimization of the MC parameters and investigations of the impact of the dose at the interface were calculated by using the beam modelled from the energy spectrum. The same spectrum was used for the simulation of the base line values of the water phantom and the non-uniformity of the CVD voxels. The beam source for the simulations presented in this chapter was the *Mohan6.spectrum* file. For the beam generated with *phase space* data, similar dose variations at detector level are expected.

Chapter IV

Experimental Validation

4.1 Introduction

This chapter contains simulations of the CVD diamond detector, with the overall aim of showing the potential that the detector has in measuring the absorbed dose at different depths inside a water phantom, and in lateral beam profile evaluation.

BEAMnrc code was used in previous work by Deloar et al. [51] to simulate a Varian 2100C linear accelerator head from Christchurch Hospital for different energies. Validation of the *phase space data* file in Deloar's work was done by comparing the percentage depth dose (PDD) curves and profiles of measured data at different

depths, with curves obtained from linear accelerator simulations for the same energy. The *phase space* file from this work, for a 10 × 10 cm^2 field size was used henceforth. In all the simulations, the same beam was used for all dose calculations.

The optimized MC parameters found in the previous chapter were utilized to investigate interface effects for different electrode materials by comparing the absorbed dose for the detector orientated perpendicular and parallel to the beam. Properties of the dose deposited in the CVD detector in the form of PDD and profiles at different depths were also investigated.

4.2 Materials and methods

The optimized *EGSnrc* input parameters used in these simulations were the *521icru.pegs4 cross section data* file and the *EXACT boundary crossing algorithm*, with the *HOWFARLESS* option turned “off”.

The source input file was the *phase space* file for the Varian 2100C linear accelerator obtained by Deloar et al. [51].

For consistency, the number of 100 million histories was kept the same. The dimension of the water phantom and the detector setup are shown in Figures 4.1 and 4.2.

The results were analyzed using the *STATDOSE* code, and the plotting programs *Xvgr/Xmgr*. The *DOSXYZ_SHOW* code was used to visualize the simulations.

4.2.1 Investigation of the interface phenomena

For a better understanding of the interface phenomena between low and high atomic number materials, the detector was investigated for two orientations, perpendicular and parallel to the beam. The interface effects were considered for detectors with electrodes made of increasing atomic number materials: aluminium (Z = 13), copper (Z = 29), silver (Z = 47), and gold (Z = 79).

Detector perpendicular to beam direction

Simulations with the detector perpendicular to the direction of the beam (Figure 4.1) were done at a depth of 5 cm along the central axis Z of the water phantom, for thicknesses of 0.07/0.2/0.07 cm for the electrode/carbon/electrode structure.

The core of the detector was considered to be a homogeneous CVD carbon which was generated by using *PEGS4* code and added to the material list of the *521icru.pegs4 cross section data* file.

The water phantom was modelled using voxels of 1.0 × 1.0 × 0.2 cm^3. Smaller voxels were used to simulate the carbon and the electrodes (dimensions of each voxel being of 1.0 × 1.0 × 0.01 cm^3), as well as the two regions before and after the detector. These regions were modelled by using a number of 13 water voxels for the area before the front electrode, with another 13 water voxels used for the area located after the back electrode. The purpose of modelling these two areas using small size voxels was to allow the program to properly show the dose variation in these critical regions.

Based on previous work by Gorka et al. [27], as well as the study undertaken in this research and validated against their work, complex interface phenomena for the

particles travelling through the media of high to low atomic number materials were expected.

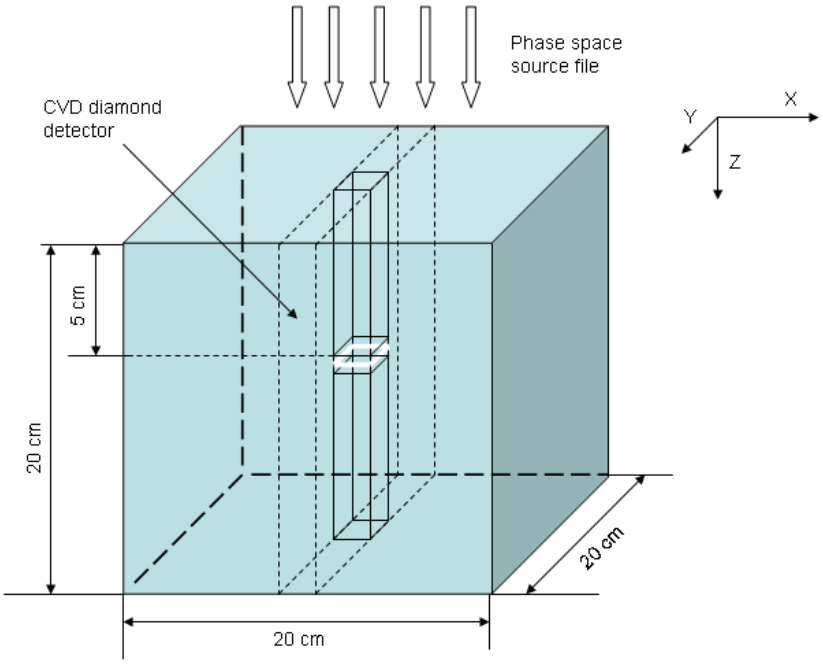

Figure 4.1 Schematic diagram showing the detector inserted perpendicular to the beam, at 5 cm depth in a 20 x 20 x 20 cm^3 water phantom with a *phase space source* file as photon beam source

Simulation results for different electrode materials will be presented as relative dose levels inside the water phantom, in the media surrounding the electrodes and through the active area.

Detector parallel to beam direction

The detector was modelled at the same 5 cm depth along the central axis of the water phantom, parallel to the beam, as shown in Figure 4.2, with the same thicknesses of 0.07/0.2/0.07 cm for the electrode/carbon/electrode structure.

As in simulations done for the detectors positioned perpendicularly to the beam, detectors with electrodes made of aluminium, copper, silver and gold were investigated. Dose levels are presented as relative absorbed dose inside the water

phantom, as well as in the detector layers and through the two areas before and after the electrodes.

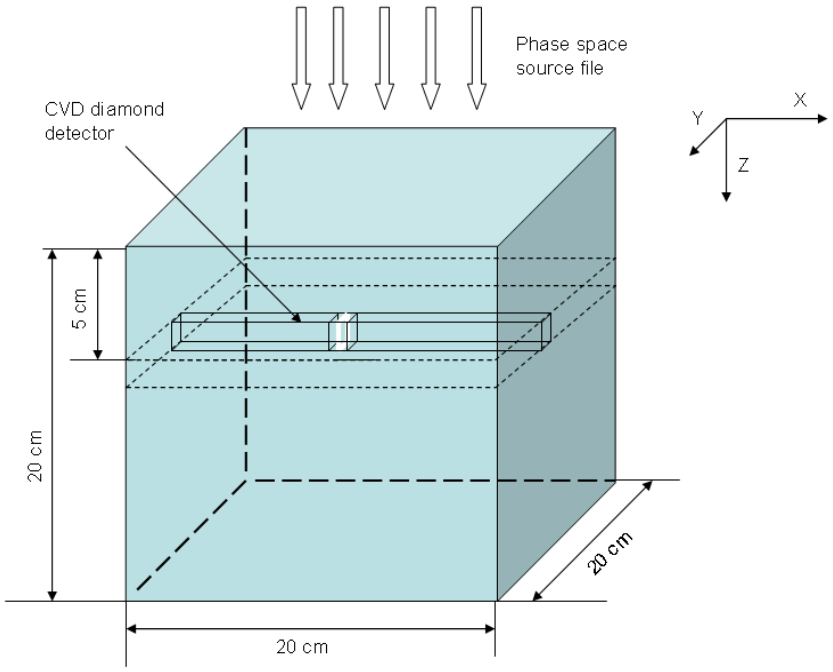

Figure 4.2 Schematic diagram showing the detector inserted parallel to the beam, at 5 cm depth in a 20 × 20 × 20 cm^3 water phantom with *phase space source* file as photon beam source

4.2.2 Comparison between simulated PDD and experimental data

In this set of experiments the CVD diamond detector was simulated at different depths in the water phantom: 1.5 cm, 5 cm, 10 cm, and 15 cm, with the detector parallel to the beam direction. The obtained PDD values were compared with experimental data measured with a Scanditronix waterproof 0.1 cm^3 RK ion chamber with interior radius of 2 mm and polarization voltage of 250 V. A Scanditronix RFA 300plus tank was used for scanning in water.

Simulations were done for a carbon layer of 0.5 × 0.5 × 0.1 cm^3, and two metal layers of 0.5 × 0.5 × 0.01 cm^3, one for each of the electrodes made of aluminium, copper, silver and gold.

The average values of the dose deposited inside the active volume of the carbon were calculated for each depth, then each of the point doses were normalized relative to the average dose calculated for the detector at 1.5 cm. This allowed the simulated doses to be compared with the PDD values obtained from the water tank. A similar procedure was followed for the evaluation of the dose profiles shown in the next section.

4.2.3 Comparison between simulated dose profiles and experimental data

Simulated dose profiles along the X direction of the water phantom were compared with experimental data. For this, detectors were modelled in seven different locations along the X direction, at distances of 0, -25, -40, -45, -48, -49, and -50 mm from the centre of the beam. Three sets of simulations at depths of 1.5 cm, 5 cm, and 10 cm inside the water phantom were performed.

All the detectors were modelled as carbon, with a size of 0.5 × 0.5 × 0.1 cm^3. Dose values were normalized relative to the maximum dose, which was determined experimentally to be at 1.5 cm.

4.3 Results and discussion

4.3.1 Investigation of the interface phenomena

Detector perpendicular to beam direction

Figure 4.3 shows the influence that the increasing atomic number of the electrode materials have on the dose absorbed in the media adjacent to the detector, and through the active area and the electrodes. The graph shows the relative dose

variation when the photon beam crosses the detector, for the four different electrode materials.

A sharp increase of the absorbed dose was measured in front of the first electrode. The highest values of the absorbed dose in each of the simulations were reached at this level of interface.

While the beam passed through the first electrode, the dose dropped as the photons were penetrating the active layer, after which it increased again in front of the second electrode. Further on, the dose has dropped almost vertically while the beam crossed through the second electrode, just to re-stabilize after passing the interface of the second electrode with the water media. At depths beyond the second electrode, as the distance from the detector increases, the dose starts to level out at values just below those measured before its penetration.

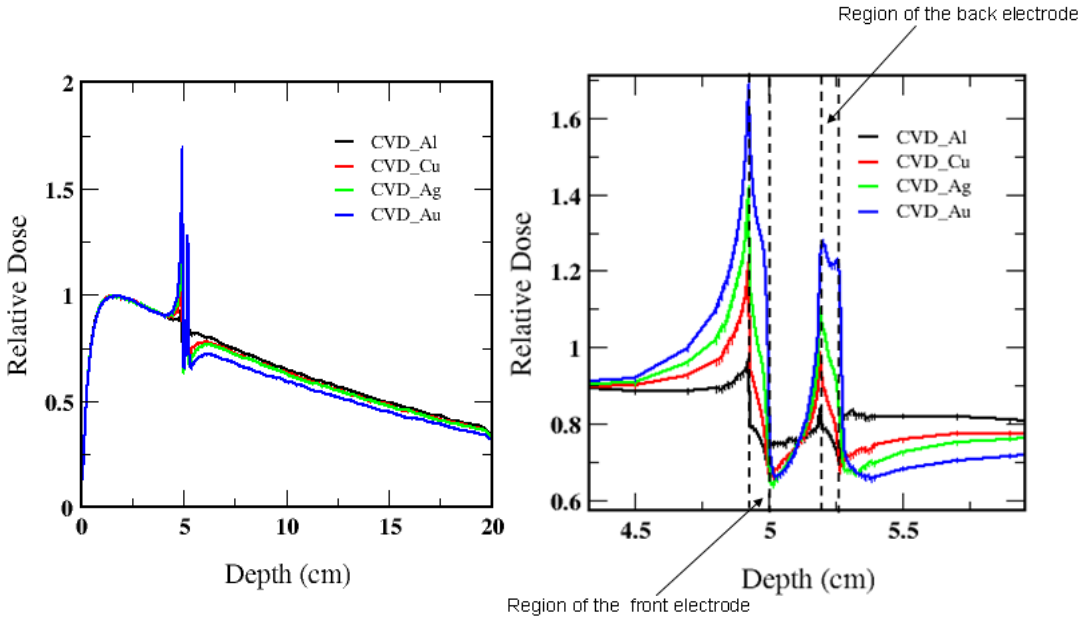

Figure 4.3 a) Percentage depth dose variation for different electrode material with the detector orientated perpendicular to the beam
b) Magnification of the region of interest

To properly compare absorbed dose levels in the region of interest shown in Figure 4.3b, all dose values were normalized to the dose at 1.5 cm.

The rapid growth of the absorbed dose at the interface with the front electrode is caused by the back scatter electrons produced during the interference of the beam with the electrode material. For the electrodes simulated as being made of the two materials having the lowest and the highest atomic numbers (Z = 13 for aluminium, Z = 79 for gold), the relative dose peaked at values of 3% below and 72% above the reference dose in water, respectively. While the photon beam crossed the electrode, the absorbed dose in these two simulations decreased rapidly to 32% and 34% below the reference dose, respectively.

The absorbed dose increased again in front of the second electrode, to 14% only below the reference dose for aluminium, and 28% above the same dose for gold. A substantial dose decrease was observed while the photon beam crossed the back electrode, at levels of 31% below the reference dose for aluminium and 35% below for gold.

In all four simulations the highest dose was of 72% above the reference, with the lowest reading dropping as low as 37% below the same reference value. Deeper in the phantom (at 6 cm and more), the relative value of the absorbed dose stabilized at values between 19% and 28% below the reference.

Detector parallel to beam direction

As shown in Figure 4.4, in simulations with the detector positioned parallel to the beam, the differences between the relative doses for the different electrode materials are much smaller than the differences observed in the previous set of four simulations (with the detector perpendicular to the beam).

The maximum variation of the relative dose for the beam crossing throughout the entire detector was of 21%, between 2% and 23% below the reference dose for the gold and aluminium electrodes, respectively (including the noise levels induced by the reduced detector voxel dimensions). This dose variation is well below the maximum relative dose difference of 109% calculated for the perpendicular detector between the highest relative dose of 72% above, and the lowest value of 37% below the reference.

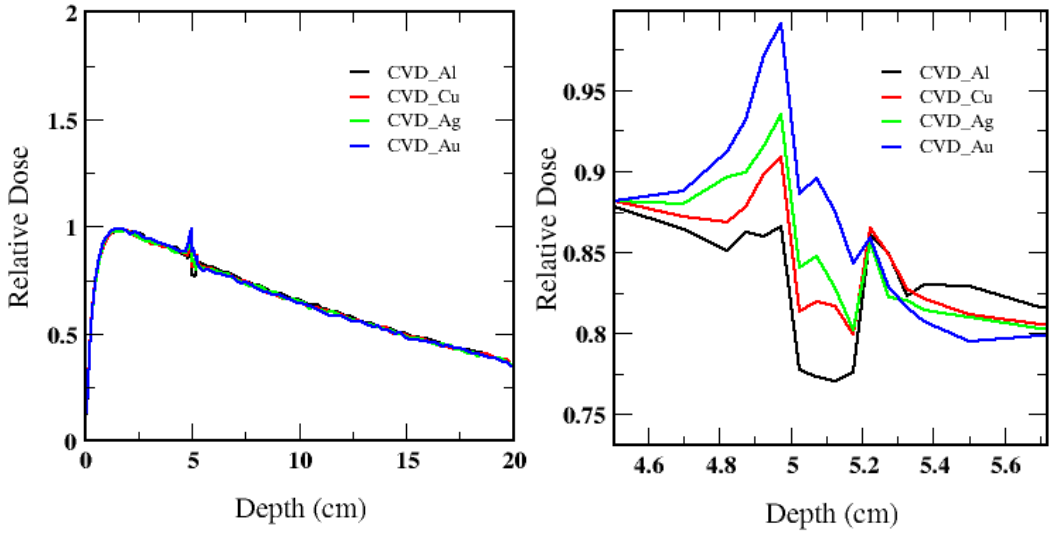

Figure 4.4 a) Percentage depth dose variation for different electrode materials with the detector orientated parallel to the beam
b) Magnification of the region of interest

Due to the parallel orientation, in these simulations the interface phenomenon is minimized. The differences between relative dose values are reduced, with the interface effects caused by the different electrode material atomic numbers being very small.

The dose through the detector in the parallel orientation presents a more stable trend than the dose through the perpendicularly positioned detector.

4.3.2 Comparison between simulated PDD and experimental data

In this set of simulations the variation of the absorbed dose in the form of PDD for the CVD detector with four different electrodes was investigated. Due to the large variations in the interface phenomena for the perpendicularly positioned detector it has been considered that the PDDs for this orientation were not worth to investigate. Therefore only PDDs for the parallel detector were studied.

Comparison between simulated PDDs using the parallel orientated detector with different electrode materials at depths of 1.5 cm, 5 cm, 10 cm and 15 cm inside the water phantom, and the experimental data obtained with the waterproof ionization chamber are shown in Figure 4.5. The results are presented as relative values normalized to their corresponding dose at 1.5 cm depth.

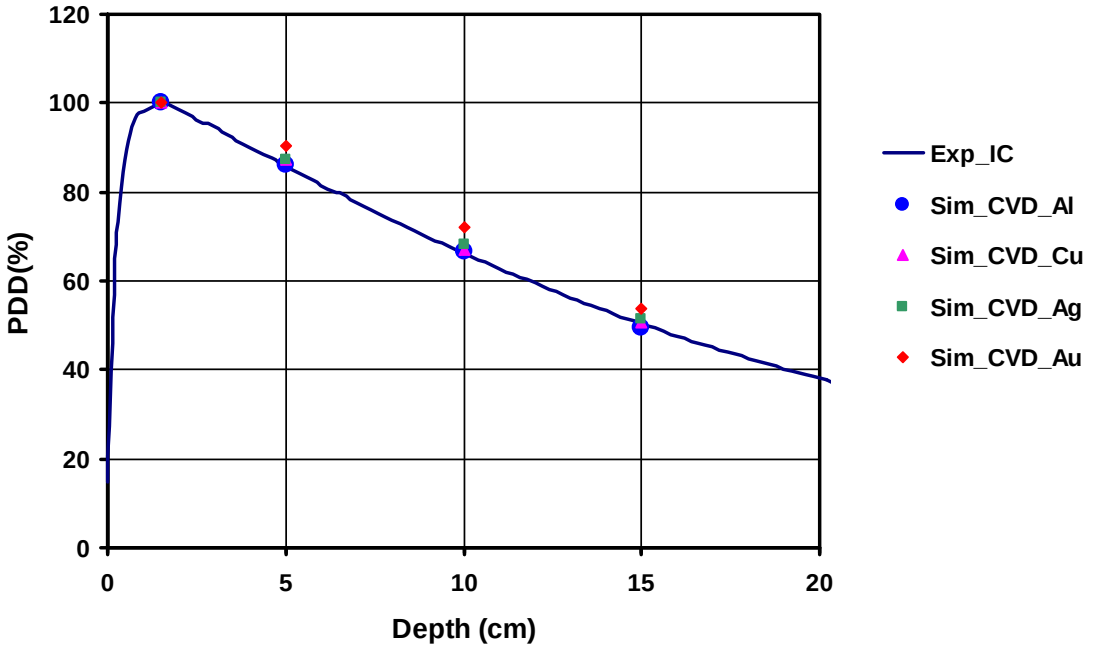

Figure 4.5 Comparison between simulated percentage depth dose obtained from the detector for different electrode materials, and the percentage depth dose obtained experimentally using the ionization chamber

Simulated PDDs of the CVD with copper and silver electrodes appeared between the PDDs for the CVD with electrodes of aluminium and gold. The deviation patterns of the PDDs for the four different electrodes showed as a function of the different material atomic number. Simulation data closest to the experimental values was obtained for the detector modelled with aluminium electrodes, while the gold electrodes presented the highest dose deviation.

The differences in the PDDs for the gold electrodes were caused by the increased scatter contribution emerging due to the high atomic number of the electrode material, and implicitly by the interface phenomenon which is amplified due to the increase of the back scatter particle perpendicularly incident to the internal surfaces of the electrodes.

Validation of the simulated PDDs shows that by avoiding the high atomic number material in the construction of the CVD diamond detector electrodes, the interface phenomena and scatter effects can be minimized. Therefore, use of electrode materials of a low atomic number is recommended.

4.3.3 Comparison between simulated dose profiles and experimental data

As shown in Figure 4.5, previous simulations indicated that the aluminium electrodes detector would produce the results closest to the experimental data measured with the ionization chamber.

In this section, dose profiles at different depths were investigated by running three more sets of simulations using the detector with aluminium electrodes. In each set, the detector orientated parallel to the beam was located in seven different positions in the (XY) plane, at depths of 1.5 cm, 5 cm, and 10 cm inside the water media. The results are shown in Figure 4.6.

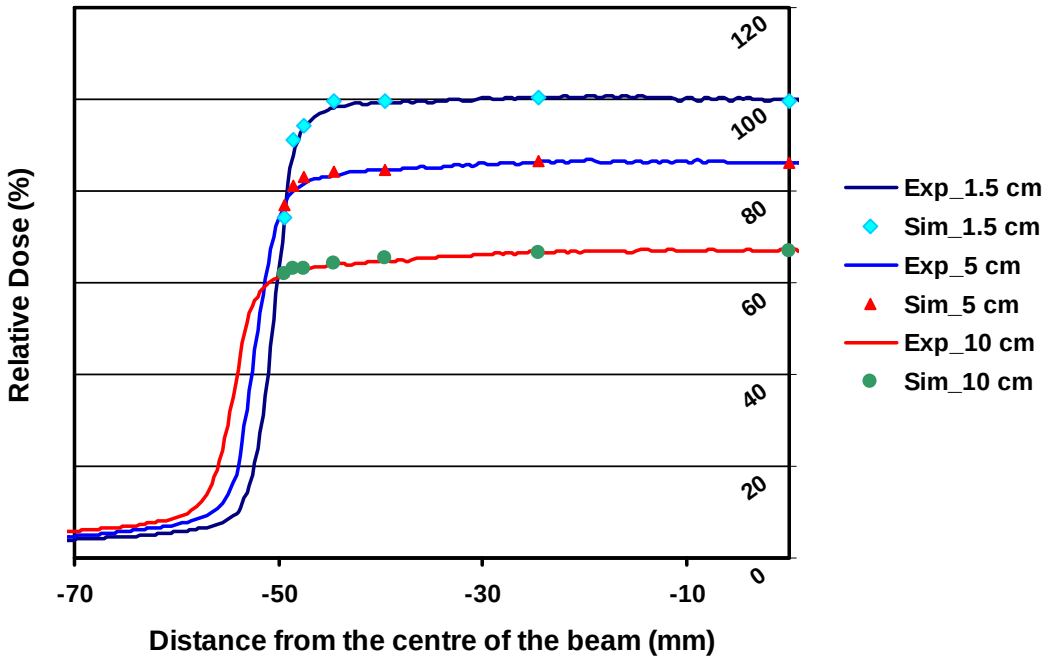

Figure 4.6 Comparison between simulated dose profiles and experimental data for detectors simulated at depths of 1.5 cm, 5 cm, and 10 cm inside the water phantom

Simulated data at the maximum distance from the centre of the beam (-50 mm) is in good agreement with the dose measured in each of the three experiments. As the distance from the detector to the centre of the beam decreases, the simulated dose is slightly overestimated in the region between -49 mm to -40 mm, with the highest variation at -45 mm.

The small differences between the simulated data and the experimental results are attributed to the very small volume of the detector placed in the water phantom modelled with relatively large voxel size. As shown in Chapter III, for the same number of histories in a setup with two different voxel dimensions the uncertainty of the calculated dose in the small voxel will be prominent.

Even though there are some variations of the simulated doses with respect to the experimental data as a whole, the simulations in each of the three depths were in good agreement with the experimental profiles.

4.4 Summary

It was found that the orientation of the detector (parallel, or perpendicular to the beam) has an important influence on the simulation output due to the interface phenomena at the face of the electrode. Parallel orientation results in better readings, with less perturbation.

At the same time, electrodes made of low (close to water) atomic number materials will provide precise readings, as the interface phenomena through these materials is smaller than the phenomena developed through higher atomic number electrodes.

Scatter will also lead to higher dose deviations in high atomic number materials. As shown in Figure 4.5, at a depth of 10 cm, a 5% higher dose was obtained for the gold electrodes, when compared to those made of aluminium.

Data for simulations with the parallel detector at 10 cm depth (Figure 4.6) showed the best agreement with the experiments.

Chapter V

Conclusions

The purpose of this research was to simulate a small dimensions CVD diamond detector for radiation dosimetry.

The physical characteristics of the detector (overall size, electrode thickness and materials, and orientation relative to the beam), as well as *EGSnrc* code transport parameters (the *cross section data*, the *boundary crossing algorithm*, and the *HOWFARLESS algorithm*) were varied to see what influence they have on the measurements of the dose through the detector and in areas adjacent to it.

The research was centred first on understanding what the capabilities of the *DOSXYZnrc* MC code are, in terms of the simulation of very small voxels. The

results revealed a high variation of the absorbed dose at the level of the detector (with small voxels) for water voxels only and default *EGSnrc* parameters.

In order to reduce these variations, the effect of different combinations of *EGSnrc* parameters was studied. For a given number of histories, the best combination was found to be the *521icru.pegs4 cross section data, EXACT boundary crossing algorithm*, with the *HOWFARLESS* option turned "off". This combination was used in further simulations to validate the model. It was during this work that a MC method was developed for the optimum *EGSnrc* parameters which will yield accurate simulation results in relatively low time frames, and which is technically viable for the use of actual computer technology.

For validation, data from simulations was compared with data from work published in the literature. During this research work interface phenomena were studied for finite detector geometry, while simulations done previously by others used to study infinite slab geometry detectors. Good agreement was found between the calculated doses in both geometries.

Simulation results were also validated against commissioning data. The dose levels calculated during the simulations were found to be in good agreement with the levels measured experimentally.

In this research a comparative study was done for the interface phenomena effects for detectors orientated in two different positions, perpendicular and parallel to the direction of the radiation beam. This was done for detectors with electrodes made of aluminium, copper, silver and gold. It was found that the amplitude of the interface phenomena for the detector perpendicular to the beam is considerably higher than the phenomena for the detector orientated parallel to the beam direction, and that the lowest dose gradient in the active area of the detector corresponds to the electrode material having the lowest atomic number.

It can be advised that in order to avoid the occurrence of high interface phenomena and high dose gradients in the active area of the detector, the electrodes should be made of low (close to water) atomic number materials, and that for improved dose evaluation the detector should be positioned parallel to the beam direction.

MC code was successfully used in the investigation of the small size radiation detector physical and dosimetrical properties. The work proved that the MC method is an ideal modelling tool for the design of reduced dimensions dosimetry devices, and is part of the theoretical base for their future design. Construction and use of the detectors will be partially based on the results presented herein.

5.1 Future Work

Having validated the model, future CVD diamond detector work should include:

1. Simulation of the detector for different electrode thicknesses, by keeping the same thickness for the active area. This will give a better understanding of the influence of the electrode thickness on the absorbed dose.

2. Energy dependency simulations for the investigation of the detector interface phenomena at different photon beam energies, i.e. 10 MV and 18 MV.

3. Simulation of the detector for different diamond layer thicknesses, to investigate the influence this has on the absorbed dose readings.

4. Modelling of the detector with geometry closer to its real configuration, i.e. with the detector including encapsulation and electrical connections.

5. Angular dependency investigations, by simulating the detector at different (other than parallel and perpendicular) orientations relative to the beam.

6. Dose linearity investigations for different rate values (50 MU/min., 100 MU/min., 150 MU/min., 200 MU / min. and 250 MU/min.).

7. Investigations of the detectors with smaller electrodes.

8. Simulations for the investigation of the detector in small radiation fields.

9. Study of the detector for different doping of the carbon film.

References

1. Ministry of Health. *Cancer is the leading cause of death* Accessed 2009 http://www.moh.govt.nz/moh.nsf/indexmh/cancer-leading-cause-of-death-11sep07.

2. Stanton R. and Stinson D., *Applied Physics for Radiation Oncology*. 1996: Medical Physics Publishing.

3. National Cancer Institute. *Cancer Mail from the National Cancer Institute*. Accessed 2009; http://imsdd.med.uni-bonn.de/cancernet/600071.html.

4. Khan F.M., *The physics of radiotherapy*. 2003: Lippincott Williams & Wilktins.

5. Taylor A. and Powell M. E. B., Intensity-modulated radiotherapy-what is it? *International Cancer Imaging Society*, 2004. 4: 68-73.

6. Podgorsak E. B., *Radiation Oncology Physics: A Handbook for Teachers and Students*, ed. Technical. 2005, Vienna: IAEA.

7. Metcalfe P., *The Physics of Radiotherapy X-Rays*. 1997: Medical Publishing.

8. Rodriguez M., Griffin S., DeWerd L., and Jeraj R., Characterization of the ADD-33 diamond detector. *Medical Physics* 2006. 34(1): 215-220.

9. De Wagter C., The ideal dosimeter for intensity modulated radiation therapy (IMRT): What is required? *Journal of Physics*, 2004. Conference series 3: 4-8.

10. Laub W. U and Wong T., The volume effect of detectors in the dosimetry of small fields used in IMRT. *Medical Physics*, 2003. 30(3): 341-346.

11. Wesermark M., Arndt J., Nilsson B., and Brahme A., Comparative dosimetry in narrow high-energy photon beams. *Physics Medicine and Biology*, 1999. 45(2000): 685-702.

12. Rustgi S. N. and Frye S. M. D., Dosimetric characterization of radiosurgical beams with a diamond detector. *Medical Physics*, 1995. 22(12): 2117-2121.

13. Burgemeister E. A. and Schouten W., The construction of a diamond detector for ionising radiation. *Radiation Protection Dosimetry*, 1983. 6(1): 145-148.

14. Prasad R. R. (1996) *Diamond Radiation Detectors*. Alameda Applied Sciences Corporation

15. Bucciolini M., Banci Buonamici F., Mazzocchi S., DeAngelis C., Onori S., and Cirrone G. A. P., Diamond detector versus silicon diode and ion chamber in photon beams of different energy and field size. *Medical Physics*, 2003. 30(8): 2149-2151.

16. Sauer O. A. and Wilbert J., Measurement of output factors for small photon beams. *Medical Physics*, 2007. 34(6): 1983-1988.

17. Laub W. U., Kaulich T. W., and Nusslin F., Energy and dose rate dependence of a diamond detector in the dosimetry of 4-25 MV photon beams. *Medical Physics*, 1997. 24(4): 535-536.

18. Kania D. R., *Diamond radiation detectors*, Advance Microtechnology Program, Lawrence Livermore National Laboratory Livermore. 135-138.

19. Vatnitsky S. M., Khrunov V. S., Fominych V. I., and Schuelell E., Diamond detector dosimetry for medical applications. *Radiation Protection Dosimetry*, 1993. 47(1): 515-518.

20. Fidanzio A., Azario L., Viola P., Ascarelli P., Cappelli E., Conte G., and Piermattei A., Photon and electron beam dosimetry with a CVD diamond detector. *Nuclear Instruments & Methods in Physics Research*, 2004. A 524: 115-123.

21. Fidanzio A. and Azario L., A preliminary dosimetric characterization of chemical vapor deposition diamond detector prototypes in photon and electron radiotherapy beams. *Medical Physics*, 2005. 32(2): 389-395.

22. PTW. *Diamond Detector*. Accessed 2008; http://www.ptw.de/diamond_detector0.html.

23. Khrunov V. S., Martynov S. S., Vatnitsky S. M., Ermakov I. A., Chervijakov A. M., Karlin D. L., Fominych V. I., and Tarbeyev Y. V., Diamond detectors in relative dosimetry of photon, electron and proton radiation fields. *Radiation Protection Dosimetry*, 1990. 33(1): 155-157.

24. Cirrone G. A. P., Cuttone G., Lo Nigro S., Mongelli V., Rafaele L., and Sabini M. G., Dosimetric characterization of CVD diamonds in photon, electron and

proton beams. *Nuclear Physics B - Procedings Supplements*, 2006. 150: 330-333.

25. Cirrone G. A. P., Cuttone G., Rafaele L., Sabini M. G., DeAngelis C., Onori S., Pacillo M., Bucciolini M., Bruzzi M., and Sciortino S., Natural and CVD type diamond detectors as dosimeters in hadrontherapy applications. *Nuclear Physics B - Proceedings Supplements*, 2003. 125: 179-183.

26. Foulon F., Bergonzo P., Jany C., Gicquel A., and Pochet T., CVD diamond detectors for radiation pulse characterisation. *Nuclear Instruments & Methods in Physics Research A*, 1996. 380: 42-45.

27. Gorka B., Nilsson B., Fernandez-Varea J. M., Svensson R., and Brahme A., Influence of electrodes on the photon energy deposition in CVD-diamond dosimeters studied with the Monte Carlo code PENELOPE. *Physics Medicine and Biology*, 2006. 51: 3607-3623.

28. Lansley S.P., Betzel G.T., Baluti F., Reinisch L., and Meyer J., Investigation of the suitability of commercially available CVD for megavoltage x-ray dosimetry. *Nuclear Instruments & Methods in Physics Research*, in press.

29. Lansley S.P., Betzel G.T., Baluti F., Lydon J., and Reinisch L. *Suitability of Synthetic Diamond Films for X-ray Dosimetry Applications*. in *Optoelectronic and Microelectronic Materials and Devices (COMMAD'08)*. 2008. Sydney, Australia.

30. Monte Carlo history for SSI. *Impact of Monte Carlo methods on scientific research*. Accessed 2008; http://www.csm.ornl.gov/ssi-expo/MChist.html.

31. Kochanski G. *Monte Carlo Simulation*. Accessed 2008; http://kochanski.org/gpk/teaching/0501Oxford/MonteCarlo.pdf.

32. Metropolis N. *The beginning of the Monte Carlo Method*. Accessed 2008; http://jackman.stanford.edu/mcmc/metropolis1.pdf.

33. Walter R. N. *History and Overview of EGS4*. Accessed 2008; http://rcwww.kek.jp/research/egs/docs/pdf/History_and_Overview.pdf.

34. Pallana S. *History of Monte Carlo Mehod*. Accessed 2008; http://www.geocities.com/CollegePark/Quad/2435/history.html.

35. Lin S. Y., Chu T. C., and Lin J. P., Monte Carlo simulation of a clinical linear accelerator. *Applied Radiation and Isotopes*, 2001. 55: 759-765.

36. Yamamoto T., Teshima T., Miyajima S., Matsumoto M., Shiomi H., Inoue T., and Hirayama H., Monte Carlo Calculation of Depth Doses for Small Field of CyberKnife*. Radiation Medicine*, 2002. 20(6): 305-310.

37. Haryanto F., Fippel M., Laub W.U., Dohm O., and Nusslin F., Investigation of photon beam output factors for conformal radiation therapy - Monte Carlo simulations and measurements*. Physics Medicine and Biology*, 2002. 47: N133-N143.

38. Kawrakow I. and Rogers D. W. O., *The EGSnrc Code System: Monte Carlo simulation of electron and photon transport*, NRC, Editor. 2000: Ottawa Canada.

39. Chin, P. W., *Monte Carlo Portal Dosimetry*. 2005, University of Wales.

40. Kawrakow I., Accurate condensed history Monte Carlo simulation of electron transport. I. EGSnrc, the new EGS4 version*. Medical Physics*, 2000. 27: 485-498.

41. Rogers D. W. O., Faddegon B. A., Ding G. X., Ma C. M., We J., and Mackie T. R., BEAM: A Monte Carlo code to simulate radiotherapy treatment units*. Medical Physics*, 1995. 22: 503-524.

42. Rogers D. W. O., Ma C. M., Ding G. X., and Walters B., *BEAM Users Manual*, NRC, Editor. 1995.

43. Hendricks J.S., *MCNPX, VERSION 2.5e*, Los Alamos National Laboratory.

44. Kawrakow I. and Fippel M., Investigation of variance reduction techniques for Monte Carlo photon dose calculation using XVMC*. Physics Medicine and Biology*, 2000. 45(2000): 2163 -2184.

45. Agostinelli S., Allison J., Amako K., and Apostolakis J., GEANT4 - a simulation toolkit*. Nuclear Instruments & Methods in Physics Research*, 2003. A 506: 250-303.

46. *The EGSnrc Code System Monte Carlo Simulation of Electron and Photon Transport*. Accessed December 2008; http://www.irs.inms.nrc.ca/EGSnrc/EGSnrc.html.

47. Walters B. R. B and Rogers D. W. O., *DOSXYZnrc Users Manual*, in *PIRS-794*. 2002: Ottawa:NRCC.

48. Nelson W. R., Hirayama H., and Rogers D. W. O., *The EGS4 Code System*, S.L.A. Center, Editor. 1985: Stanford, California.

49. Kawrakow I., *The dose visualization tool dosxyz show*, in *Ionizing Radiation Standards*, N.R.C. Canada, Editor.

50. Mohan R., Chui C., and Lidofsky L., Energy and angular distributions of photons from medical linear accelerator*. Medical Physics*, 1985. 12: 592-597.

51. Deloar H. M., Griffin J., Bird M., Wilder B., Morgan S., Hsieh W. L., Sorell G., and Knieda E., *Evaluation of clinical dose distributions using Monte Carlo methods*, in *The World Congress on Medical Physics and Biomedical Engineering,* 2006, Publisher Springer: Seoul, Korea. 1840-1841.